Publications of the Astronomical Society of the Pacific, 138:034101 (26pp), 2026 March https://doi.org/10.1088/1538-3873/ae4539

LIGO/Virgo/KAGRA Neutron Star Merger Candidate S250206dm: Zwicky Transient Facility Observations

Tomás Ahumada[1], Shreya Anand[2,3,29], Mattia Bulla[4,5,6], Vaidehi Gupta[7], Mansi Kasliwal[1], Robert Stein[8,9,10], Viraj Karambelkar[1], Eric C. Bellm[11], Theophile Jegou du Laz[1], Michael W. Coughlin[7], Igor Andreoni[12], Smaranika Banerjee[13], Aleksandra Bochenek[14], K-Ryan Hinds[14], Lei Hu[15], Antonella Palmese[15], Daniel Perley[14], Natalya Pletskova[16], Anirudh Salgundi[17], Avinash Singh[13], Jesper Sollerman[18], Vishwajeet Swain[17], Avery Wold[19], Varun Bhalerao[20], S. Bradley Cenko[9,10], David O. Cook[21], Chris Copperwheat[14], Matthew Graham[1], David L. Kaplan[22], Leo P. Singer[10], Niharika Sravan[16], Malte Busmann[23], Julius Gassert[23], Daniel Gruen[23,24], Julian Sommer[23], Yajie Zhang[23], Ariel Amsellem[15], Tomás Cabrera[15], Xander J. Hall[15], Keerthi Kunnumkai[15], Brendan O'Connor[15], Tyler Barna[7], Felipe Fontinele Nunes[7,25,26], Andrew Toivonen[7], Argyro Sasli[7], Frank J. Masci[21], Tracy X. Chen[21], Richard Dekany[27], Josiah Purdum[27], Antoine Le Calloch[7], G. C. Anupama[28], and Sudhanshu Barway[28]

[1] Cahill Center for Astrophysics, California Institute of Technology, MC 249-17, 1216 E California Boulevard, Pasadena, CA 91125, USA
[2] Kavli Institute for Particle Astrophysics and Cosmology, Stanford University, 452 Lomita Mall, Stanford, CA 94305, USA
[3] Department of Astronomy, University of California, Berkeley, CA 94720-3411, USA
[4] Department of Physics and Earth Science, University of Ferrara, via Saragat 1, I-44122 Ferrara, Italy
[5] INFN, Sezione di Ferrara, via Saragat 1, I-44122 Ferrara, Italy
[6] INAF, Osservatorio Astronomico d'Abruzzo, via Mentore Maggini snc, 64100 Teramo, Italy
[7] School of Physics and Astronomy, University of Minnesota, Minneapolis, MN 55455, USA
[8] Department of Astronomy, University of Maryland, College Park, MD 20742, USA
[9] Joint Space-Science Institute, University of Maryland, College Park, MD 20742, USA
[10] Astrophysics Science Division, NASA Goddard Space Flight Center, MC 661, Greenbelt, MD 20771, USA
[11] DIRAC Institute, Department of Astronomy, University of Washington, 3910 15th Avenue NE, Seattle, WA 98195, USA
[12] Department of Physics and Astronomy, University of North Carolina, Chapel Hill, NC 27599, USA
[13] The Oskar Klein Centre, Department of Astronomy, Stockholm University, AlbaNova, SE-10691 Stockholm, Sweden
[14] Astrophysics Research Institute, IC 2, Liverpool Science Park, 146 Brownlow Hill, Liverpool L3 5RF, UK
[15] McWilliams Center for Cosmology and Astrophysics, Department of Physics, Carnegie Mellon University, 5000 Forbes Avenue, Pittsburgh, PA 15213, USA
[16] Department of Physics, Drexel University, Philadelphia, PA 19104, USA
[17] Department of Physics, IIT Bombay, Powai, Mumbai 400076, India
[18] The Oskar Klein Centre, Department of Astronomy, Albanova, Stockholm University, SE-106 91 Stockholm, Sweden
[19] IPAC, California Institute of Technology, 1216 E. California Blvd, Pasadena, CA 91125, USA
[20] Department of Physics, Indian Institute of Technology Bombay, Powai 400 076, India
[21] IPAC, California Institute of Technology, 1200 E. California Blvd, Pasadena, CA 91125, USA
[22] Department of Physics, University of Wisconsin-Milwaukee, P.O. Box 413, Milwaukee, WI 53201, USA
[23] University Observatory, Faculty of Physics, Ludwig-Maximilians-Universität, Scheinerstr. 1, 81679 Munich, Germany
[24] Excellence Cluster ORIGINS, Boltzmannstr. 2, 85748 Garching, Germany
[25] NSF Institute on Accelerated AI Algorithms for Data-Driven Discovery (A3D3), MIT, Cambridge, MA 02139, USA
[26] University of Minnesota, Minneapolis, MN 55455, USA
[27] Caltech Optical Observatories, California Institute of Technology, Pasadena, CA 91125, USA
[28] Indian Institute of Astrophysics, 2nd Block 100 Feet Rd, Koramangala Bangalore 560034, India
Received 2026 February 4; accepted 2026 February 12; published 2026 March 10

Abstract

We present the searches conducted with the Zwicky Transient Facility (ZTF) in response to S250206dm, a bona fide event with an online false alarm rate of one in 25 yr, detected by the International Gravitational Wave Network. Although the event is significant, the nature of the compact objects involved remains unclear, with at least one likely neutron star. ZTF covered 68% of the last refined Bilby localization region, though we did not identify any likely optical counterpart. We describe the ZTF strategy, potential candidates, and the observations that helped rule out candidates, including sources circulated by other collaborations. Similar to Ahumada et al.,

[29] LSST-DA Catalyst Postdoctoral Fellow.

we perform a frequentist analysis, using `simsurvey`, as well as Bayesian analysis, using `nimbus`, to quantify the efficiency of our searches. We find that, given the nominal up-to-date distance to this event of 373 ± 104 Mpc, our efficiencies are above 10% for KNe brighter than -17.5 absolute magnitude. Assuming the optical counterpart known as kilonova (KN) lies within the ZTF footprint, our limits constrain the brightest end of the KN parameter space. Through dedicated radiative transfer simulations of KNe from binary neutron star (BNS) and black hole–neutron star mergers, we exclude parts of the BNS KN parameter space. Up to 35% of the models with high wind ejecta mass ($M_{\rm wind} \approx 0.13\,M_{\odot}$) are ruled out when viewed face-on ($\cos\theta_{\rm obs} = 1.0$). Finally, we present a joint analysis using the combined coverage from ZTF and the Gravitational Wave Multimessenger Dark Energy Camera Survey. The joint observations cover 73% of the Bilby localization region, and the combined efficiency has a stronger impact on rising and slowly fading models, allowing us to rule out 55% of the high-mass KN models viewed face-on.

Unified Astronomy Thesaurus concepts: Gravitational waves (678); Nucleosynthesis (1131); Compact binary stars (283); Optical observation (1169); Neutron stars (1108)

1. Introduction

The fourth observing run of the International Gravitational Wave Network (IGWN) re-started operations after a commissioning break between 2024 January and April, detecting more than 99 binary black hole (BBH) merger candidates and one merger with confident presence of a neutron star (NS): S250206dm. This builds on previous successful runs, that to date sum over 102 BBH mergers and 6 mergers involving an NS (Abbott et al. 2023). The most studied gravitational wave (GW) detection, GW170817, was discovered in coincidence with a short gamma-ray burst (sGRB), an afterglow, and a kilonova (KN), opening a new window into multi-messenger astronomy (MMA; Abbott et al. 2017a, 2017b; Goldstein et al. 2017). The subsequent study of the KN unequivocally revealed the presence of heavy elements, produced through *r*-process nucleosynthesis, and the study of the afterglow has allowed for the discovery of super-luminal motion and helped constrain the geometry of the system (Coulter et al. 2017; Drout et al. 2017; Evans et al. 2017; Haggard et al. 2017; Hallinan et al. 2017; Kasen et al. 2017; Kasliwal et al. 2017; Lipunov et al. 2017; Margutti et al. 2017; Soares-Santos et al. 2017; Troja et al. 2017; Utsumi et al. 2017; Valenti et al. 2017; Arcavi 2018; Mooley et al. 2018, 2022; Pozanenko et al. 2018; Kasliwal et al. 2019; Makhathini et al. 2021; Balasubramanian et al. 2022).

Due to the plethora of scientific studies that GW170817 has enabled, multiple collaborations have developed complex responses to IGWN triggers. Particularly in the optical and near-infrared (NIR), collaborations such as the Asteroid Terrestrial-impact Last Alert System (ATLAS), the All-Sky Automated Survey for Supernovae (ASAS-SN), Gravitational Wave MultiMessenger DECam Survey (GW-MMADS), the Gravitational-wave Optical Transient Observer (GOTO), the Wide-Field Infrared Transient Explorer (WINTER), and the Panoramic Survey Telescope and Rapid Response System (Pan-STARRS), among others, have all performed observations of the GW regions (Shappee et al. 2014; Chambers et al. 2016; Lipunov et al. 2017; Soares-Santos et al. 2017; Tonry et al. 2018; Lundquist et al. 2019; Antier et al. 2020; Gompertz et al. 2020; Levan 2020; Hu et al. 2023; Paek et al. 2024; Frostig et al. 2025). Despite all efforts including extensive tiling and galaxy-targeted searches, no confidently associated electromagnetic counterpart has been detected (Andreoni et al. 2019; Coughlin et al. 2019b; Goldstein et al. 2019; Andreoni et al. 2020; Antier et al. 2020; Kasliwal et al. 2020; Morgan et al. 2020; Vieira et al. 2020; Alexander et al. 2021; de Wet et al. 2021; Kilpatrick et al. 2021; Thakur et al. 2021; Dobie et al. 2022; Rastinejad et al. 2022; Tucker et al. 2022; Cabrera et al. 2024; Pillas et al. 2025).

The Zwicky Transient Facility (ZTF; Bellm et al. 2019; Graham et al. 2019; Dekany et al. 2020), mounted on the Samuel Oschin 48 inch Telescope at Palomar Observatory, is a public-private project that nominally covers the entire northern night sky in *g*, *r*, and *i* band every two nights. The high cadence of the public survey allows ZTF to have one of the most complete records of the dynamic optical sky, and enables the discovery of transients at early stages. The large field of view (FoV) of ZTF, of 47 square degrees additionally grants ZTF with the capacity to perform rapid searches of relativistic transients, such as GRBs (Coughlin et al. 2018; Ahumada et al. 2022) and GW events (Coughlin et al. 2019a; Kasliwal et al. 2020; Anand et al. 2021; Ahumada et al. 2024) across thousands of square degrees. These searches have led to the discovery of multiple afterglows, including the shortest gamma-ray burst linked to a collapsar and an orphan afterglow detected during the IGWN third observing run (O3) (Ahumada et al. 2021; Perley et al. 2025).

Throughout this paper, we discuss the follow-up of the high-significance event candidate S250206dm, describing the GW event in Section 2, the follow-up strategy of ZTF in Section 3, the candidate vetting strategy in Section 4, and we discuss the implications of our non-detections in Section 5. In Section 6, we show a joint analysis with observations from the Gravitational Wave Multimessenger Dark Energy Camera

Survey (GW-MMADS; PI. Andreoni & Palmese), which are presented in the companion paper (Hu et al. 2025), and an extensive analysis of the ZTF candidates and other candidates announced through the Transient Name Server (TNS) is presented in Appendix C.

2. S250206dm

On 2025 February 6 21:25:44 UTC IGWN detected a candidate merger of two compact objects, with a false alarm rate (FAR) of 1 in 25.01 yr. The event classification probabilities were reported in the GCN circular as 55% NSBH, 37% BNS, and 8% Terrestrial (Ligo Scientific Collaboration et al. 2025a). Assuming the GW event is of astrophysical origin, the machine learning inference on the GW data (Chatterjee et al. 2020) shows that the merger had at least one NS involved (HasNS = 100%), a 63% probability of having a compact object (HasMassGap) in the mass gap (3–5 $M_{\odot}$), and 30% of leaving remnant material to power a KN (HasRemnant) (Ligo Scientific Collaboration et al. 2025a).

The initial localization by BAYESTAR (Singer & Price 2016) covered 2139 sq. deg., distributed between a northern (decl. $> -30°$) and a southern lobe (decl. $< -30°$), containing respectively 73% and 27% of the total probability (Ligo Scientific Collaboration et al. 2025b). The localization was updated several times, and the final map, produced by Bilby (Ashton et al. 2019; Morisaki et al. 2023) and circulated 1.5 days after the event, featured a more compact northern and southern lobe. The majority of the probability shifted to the northern lobe, which contained 78% of the probability, while the southern lobe contained the remaining 22% (Ligo Scientific Collaboration et al. 2025c). In the most up-to-date localization, the 50% and 90% credible region (c.r.) covered 38 sq. deg, and 547 sq.deg.

3. ZTF Follow-up Campaign

3.1. Observing Plan

ZTF observations of the GW skymap started on UT 2025 February 8 02:21 UTC—29 hr after the merger, due to poor weather. ZTF observations are conducted on a pre-defined grid of fields, and the GW region included ZTF fields that were setting early. In order to accommodate a larger number of fields, we decided to slice the GW localization in right ascension (RA) and feed four separate regions to the scheduler optimizer `gwemopt` (Coughlin et al. 2018). The RA slices were the following: from 22 hr to 0 hr, from 0 hr to 2 hr , from 2 hr to 5 hr and from 7 hr to 21 hr . For all these regions, we scheduled a sequence of 300 s exposures in *r*, *g*, and *r* band for our first night, and a sequence of 300 s exposures in *g*, *r*, *i* band for the following nights. In order to account for the chip gaps in the ZTF fields, we scheduled observations using fields in both the primary and secondary grid, as they have complementary coverage of the ZTF fields. The schedule was repeated over the course of 9 nights. The full details of the pointings are available on TreasureMap (Wyatt et al. 2020). Within 9 days, a total of 68% of the probability enclosed within the GW skymap was observed with ZTF at least once, while 64% of the total probability was observed at least twice (see coverage in Figure 1, and the magnitude evolution in Figure 4).

3.2. Candidate Vetting

ZTF observed the S250206dm region for nine consecutive nights. Each night, the ZTF pipeline (Masci et al. 2019), operated at the Infrared Processing and Analysis Center (IPAC[30]), processes, calibrates, and performs image subtraction in near real-time. Any flux deviation exceeding 5σ from the reference image produces an *alert* (Patterson et al. 2019), which includes metadata on the transient, such as its lightcurve history, a real-bogus score (Duev et al. 2019), and other relevant information.

We then query the ZTF stream of alerts using Kowalski (Kasliwal et al. 2020) through Fritz (van der Walt et al. 2019; Coughlin et al. 2023). Our criteria for candidate selection start with an automated filtering scheme described in this paragraph. We select transients that have a positive residual after image subtraction with respect to the reference image, and a deep learning real-bogus score (Duev et al. 2019) greater than 0.3 to differentiate between real astrophysical sources and artifacts. To avoid contamination from stars, we require transients to be located more than 3″ away from sources classified as probable stars by a morphology-based classifier (Tachibana & Miller 2018) applied to sources detected by Pan-STARRS (PS1; Chambers et al. 2016). We request a minimum of two detections separated by at least 15 minutes to remove most moving objects and cosmic rays. To reduce the influence of artifacts from bright stars, we find from experience that sources must be located more than 20″ from any object with a magnitude less than 15. We exclude sources that show activity before the GW event, as KNe and relativistic afterglows are only expected to occur after the merger, and finally, we require the candidate to lie within the 95% contour of the latest and most up-to-date GW skymap.

For the ZTF sources that pass the automated alert filtering, we further cross-match the candidates to the Minor Planet Center to flag known asteroids, and we cross-match to WISE to reject AGNs using their WISE colors (Wright et al. 2010). We also run forced photometry on ZTF images (Masci et al. 2019) and require that there are no detections before the GW trigger.

In addition to Fritz, we queried the *Kowalski* database using the `emgwcave`[31] Python script, which retrieves candidates based on similar cuts to those mentioned earlier. `emgwcave`

[30] https://www.ipac.caltech.edu/
[31] https://github.com/virajkaram/emgwcave

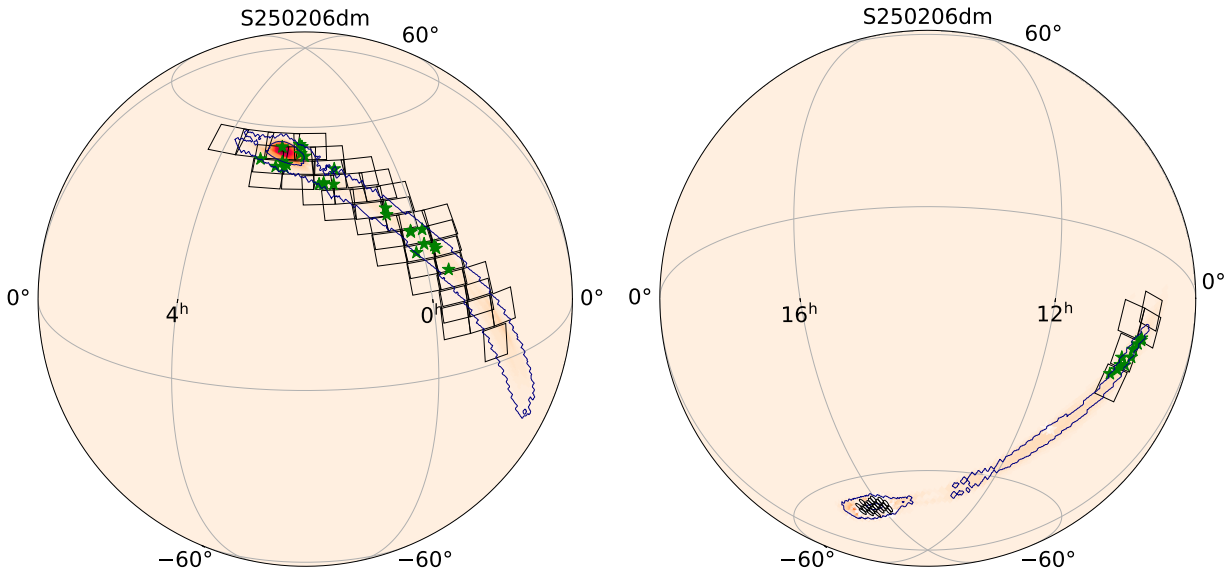

Figure 1. Localization of the high-significance event S250206dm, overlaid with the ZTF tiles (black squares), the GW-MMADS tiles (black circles), and the 90% probability contour (navy). The green stars represent transients reported publicly through TNS that were accessible from Palomar, while the white stars indicate candidates that were not accessible from Palomar.

offers added flexibility, allowing for easy modifications to the queries.

Next, we performed an independent search using the `nuztf`[32] Python package (Stein et al. 2023b), originally developed for the ZTF Neutrino Follow-Up Program (Stein et al. 2023a). The `nuztf` package utilizes the `AMPEL` framework for candidate filtering (Nordin et al. 2019) and retrieves ZTF data with minimal latency from the `AMPEL` broker data archive (Nordin et al. 2019). We applied selection criteria similar to those outlined previously, followed by automated cross-matching with various multi-wavelength catalogs to identify potential variable AGN or stars. Additionally, `nuztf` uses ZTF observation logs from IPAC to calculate the survey coverage of a skymap, factoring in chip gaps and processing failures.

Lastly, we utilized the `ZTFReST` infrastructure (Andreoni et al. 2021) to retrieve candidates. `ZTFReST` is an open-source tool for flagging fast-fading transients based on ZTF alert photometry and forced photometry (Yao et al. 2020).

The described selection criteria resulted in 13 candidates from the ZTF stream. All candidates were identified in the Fritz, `emgwcave` and `nuztf` searches, while only the fast-evolving ones appeared in the ZTFReST search, as the latter filters out slow-evolving transients ($\Delta m/\Delta t < 0.3$ mag day^{-1}). Candidates discovered after the first two nights of observations were circulated via GCN (Ahumada et al. 2025), whereas the remaining ones were reported to the Transient Name Server (TNS). The full list of ZTF candidates is shown in Table 1, and detailed descriptions for them can be found in Appendix C.

[32] https://github.com/desy-multimessenger/nuztf

To determine whether a candidate is related to the GW event, we rely on further analysis to reach one of our rejection criteria. When available, we examine the spectra of the transient and derive a classification by comparing the spectra to various known transient types, as well as KN models from Kasen et al. (2017), Bulla (2019) and Anand et al. (2021). If the source fades beyond spectroscopic limits, we use the redshift of the host to assess whether it falls within the GW volume. Alternatively, we cross-match our sources with Gaia (Gaia Collaboration 2018) and classify as *stellar* the sources within 2″ of a Gaia object with significant proper motion ($>3\sigma$). We expect stellar sources to pass our Gaia filter as the observations of ZTF reach deeper limits than the Gaia survey, which is complete to $G \approx 20$ mag (Boubert & Everall 2020). We run forced photometry over the entire history of the ZTF survey, and sources with previous detections are classified as *old*. For sources that cannot be ruled out, we request further photometric follow-up and compare the photometric evolution of the sources to KN models (Kasen et al. 2017; Bulla 2019). We classify sources as *slow* if their evolution does not align with KN model predictions.

All ZTF candidates were ruled out as potential counterparts to S250206dm based on the criteria described above.

3.3. Candidates from other Facilities

Multiple facilities conducted searches of counterparts to S250206dm. Candidates including coincident fast radio bursts (FRBs; Chime/Frb Collaboration 2025), neutrinos (IceCube Collaboration 2025), and X-ray transients (Li et al. 2025). ZTF

observations covered the regions associated with the FRB, neutrino, and Einstein Probe (EP) candidates; however, no optical counterparts were identified (see Appendix A) either in the ZTF images nor in the ZTF data stream.

Additionally, a number of optical candidates were circulated through the General Coordinate Network (GCN) and TNS (Ackley et al. 2025; Becerra et al. 2025; Busmann et al. 2025a; Cabrera et al. 2025; Chen et al. 2025a, 2025b; Coulter et al. 2025; Frostig et al. 2025; Fortin et al. 2025; Freeburn et al. 2025; Hosseinzadeh et al. 2025; Huber et al. 2025b; Lipunov et al. 2025; Liu et al. 2025; Paek et al. 2025; Smith et al. 2025; Steeghs et al. 2025; Stein et al. 2025; Watson et al. 2025; Young et al. 2025). In order to vet the optical candidates circulated through TNS, we used ZTF and facilities in the GROWTH collaboration (see Appendix B and Kasliwal et al. 2019) for follow-up. We focused on the candidates in the northern lobe, as these are accessible from Palomar Observatory and partner facilities in the northern hemisphere. We direct the reader to Hu et al. (2025) for an analysis of the candidates in the southern lobe of the skymap. Following the same rejection criteria discussed for ZTF candidates (e.g., spectral classification, photometric follow-up, catalog crossmatching), we are able to rule out 15 of the 22 candidates in the northern region. We additionally used the photometric redshifts of the host galaxies to assess whether the associated candidates fall within the predictions of the KN model grid. We determine the host association based on angular separation solely, cross-matching galaxies with transients using a 150 kpc radius for each galaxy. We found that one candidate exhibited a luminosity inconsistent with the models. The photometric redshifts were obtained from either SDSS (Beck et al. 2016) or the Legacy Survey (Zhou et al. 2021), depending on availability. These redshifts were not used to rule out sources, but rather as a proxy to evaluate whether the observed brightness is consistent with model expectations.

We cannot rule out seven candidates: AT2025bcc, AT2025bey, AT2025bbp, AT2025bah, AT2025bam, AT2025bce, and AT2025baf. A summary of the follow-up and analysis of candidates detected by other facilities can be found in Table 2 and a thorough description of each source in Appendix C. Given the lack of confirmation of a KN through public channels, in this paper and the following analysis, we assume these candidates are not counterparts to S250206dm.

4. ZTF Observation

In this section, we assess the efficiency of the ZTF search for an optical counterpart to S250206dm. Additionally, we present an updated analysis that includes high-significance (FAR $> 1\,\mathrm{yr}^{-1}$) events bearing an NS (either HasNS > 0.1, $P_{\mathrm{BNS}} > 0.1$, or $P_{\mathrm{NSBH}} > 0.1$) detected during the first part of the fourth observing run (O4a) of the IGWN. We also incorporate the confirmed astrophysical events from the third IGWN observing run (O3) into the analysis. To do so, we follow the methodology described in Ahumada et al. (2024), and we apply both a Bayesian and a frequentist approach. Using the ZTF observations, we constrain the KN luminosity function based on various assumptions.

4.1. Efficiencies

As described in previous studies (Kasliwal et al. 2020; Ahumada et al. 2024) we determine the efficacy of our searches in detecting a KN counterpart to S250206dm using two different approaches. Our frequentist approach, `simsurvey`, quantifies the efficiency with which our observations within the GW skymap would detect a KN with a particular initial absolute magnitude, M_0, and evolution rate, α, or whose lightcurve evolution is described by a KN model. With our Bayesian approach, `nimbus`, we calculate the posterior probability of a KN of a particular M_0 and α, in the GW skymap given our ZTF observations. This approach takes into account the probability that the GW event was astrophysical in origin. These complementary analyses allow us to place constraints on the properties of a potential KN associated with S250206dm. Additionally, for both analyses we show the results of the S250206dm campaign and the cumulative combined results, taking into consideration all the high-significant GW events during O3 and O4.

`simsurvey` takes as inputs ZTF pointings (the area covered), limiting magnitudes, and the GW skymap, and simulates KN lightcurves as would be observed by ZTF within the skymap. The detection efficiency, defined as fraction of KNe detected among all simulated KNe, can be a proxy for ZTF's performance in conducting these KN searches.

Similar to `simsurvey` analyses conducted in previous studies (Kasliwal et al. 2020; Ahumada et al. 2024), we calculate the efficiency with which our ZTF observations can recover KNe described by simple linear evolution models (*tophat*), and KNe from BNS mergers derived with *Bulla* models from POSSIS (Bulla 2019; Dietrich et al. 2020), *Kasen* models (Kasen et al. 2017), and *Banerjee* models (Banerjee et al. 2022). We note that we do not include KNe from NSBH mergers as these are not constrained by our observations, as they are faitner than our limits (see bottom panels in Figure 4). First, adopting a model-agnostic approach, we simulate KNe with a range of M_0 and α within the skymap of S250206dm. For each combination of M_0 and α, we simulate 10,000 KNe and calculate the single detection efficiency with ZTF. Our results are shown in Figure 2. Our ZTF limits for this event are most sensitive to rising transients and fading transients brighter than $M \sim -18$ mag. However, our detection efficiency for a GW170817-like KN is $< 1\%$; thus our observations were not sensitive to KNe fainter than GW170817.

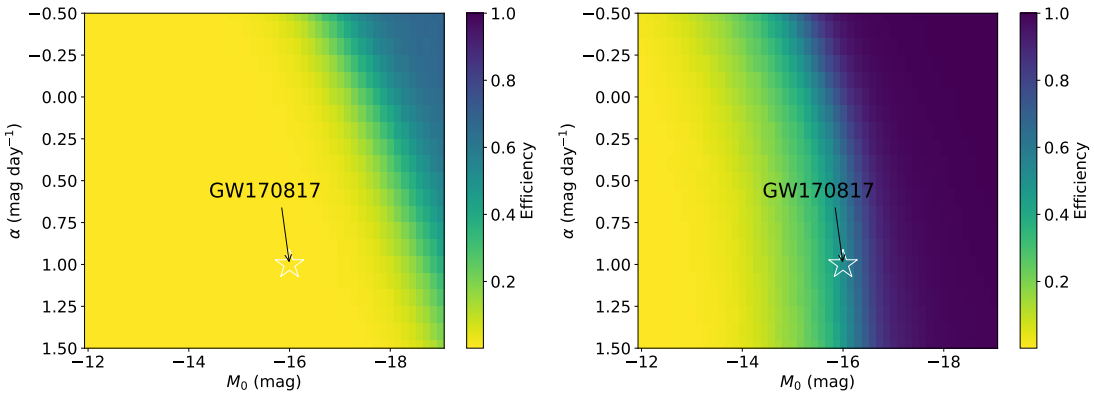

Figure 2. Kilonova single-detection efficiency with `simsurvey` for the *Tophat* model evolution for (left) S250206dm and (right) for the combined set of GW triggers: S250206dm, S230518h, S230627c, S230731an, S231113bw, GW230529, GW200115, GW200105, GW190814, GW190426, and GW190425. The color bar shows the fraction of sources detected once versus the number of sources ingested in the GW volume. We mark the position of a GW170817-like KN on this plot. The ZTF efficiency of recovering a GW170817-like KN in the skymap of S250206dm is <1% (left) while for the combined set of events the efficiency is 36%.

Given the median depths achieved on each night of observations for S250206dm, we calculate the detection efficiency for the brightest KN model in each grid we consider. Since our full set of *tophat* models does not represent the realistic range of absolute magnitudes and evolution rates expected for a KN, we choose a model with a similar peak absolute magnitude to the brightest model in the *Bulla* grid ($M_0 \approx -17.6$ mag). For the brightest *Bulla* (*Kasen*) [*Banerjee*] model with a total *r*-process ejecta mass of 0.15 (0.10) [0.05] $M_\odot$ and a peak absolute magnitude of $M_0 \approx -17.6$ (-17.0) [-16.4] mag, our ZTF detection efficiency is 15 (6) [4]%. For the corresponding *tophat* model with $M_0 = -17.6$ mag and $\alpha = 0.5$ mag day^{-1}, we achieve 10% efficiency with ZTF.

In addition, we determine the joint single-detection and filtered efficiencies for GW170817 across all significant NS merger event candidates released thus far: S250206dm, S230518h, S230627c, S230731an, S231113bw, GW230529, GW200115, GW200105, GW190814, GW190426, and GW190425. We note we consider significant events that have a FAR $< 1\,\mathrm{yr}^{-1}$, and one of the following: $P_{\rm BNS} > 0.1$, $P_{\rm NSBH} > 0.1$, or HasNS > 0.1. We note that the joint `simsurvey` analysis treats all the events equally, and focuses on measuring the ability of ZTF to detect KN. By combining the efficiencies, we measure how many KN are recovered with ZTF in all the campaigns.

Our filtering criteria for simsurvey requires two 5σ detections with ZTF separated by 15 minutes. Our joint single-detection (filtered) efficiency for a GW170817-like KN is 39 (36)% with the *Bulla* model, 38 (35)% with the *Kasen* model, 22 (20)% with the Banerjee model, and 53 (36)% with the *tophat* model. The addition of S250206dm changes the overall joint single-detection/filtered efficiency for a GW170817-like KN by $\lesssim$1% from Ahumada et al. (2024), for all models considered. However, our ZTF limits for this event contribute towards constraining the bright end of the KN luminosity function.

`nimbus` (Mohite et al. 2022) is a hierarchical Bayesian Inference framework model that integrates ZTF observations across all bands, the 3D GW skymap, and the extinction values for each field. The software injects observation parameters such as time stamps, limiting magnitudes, filter information, and the observation coordinates for three days from the merger time. `nimbus` treats observations across multiple filters as a single, unified lightcurve by assuming a shared color evolution, and uses this "average-band" for our calculations. We note that this approach ignores the physics information that different bandpasses bring, making this measurement only relying in an average evolution rate. `nimbus` computes the posterior probability ($P_{\rm nimbus}$) of a KN given the ZTF observations within the GW skymap. It then combines this posterior with the probability of the event's localization within each field to calculate the log-posterior values for each observation. `nimbus` additionally incorporates the probability that the event is of astrophysical origin, $p_{\rm astro}$, as well as the fractional sky coverage of the event by ZTF. for a more detailed explanation of the Appendix E, as well as . KN parameters for a model lightcurve can be constrained using the posterior probability derived by `nimbus`.

The $p_{\rm astro}$ value for S250206dm is 0.92, and ZTF covered 68% of the total skymap which allows for a significant posterior probability and results in constraints for the brighter KN models. Figure 3 (left) shows the posterior probability for S250206dm. The combinations of peak magnitude and M_0 evolution rate α with a higher posterior value constitute the preferred parameter space, while those with a lower posterior value are less favored. Integrating the results for S250206dm with the posterior probabilities for events from the O4a run, Figure 3 (right) shows the combined posterior probability for all events that have been considered significant: S250206dm,

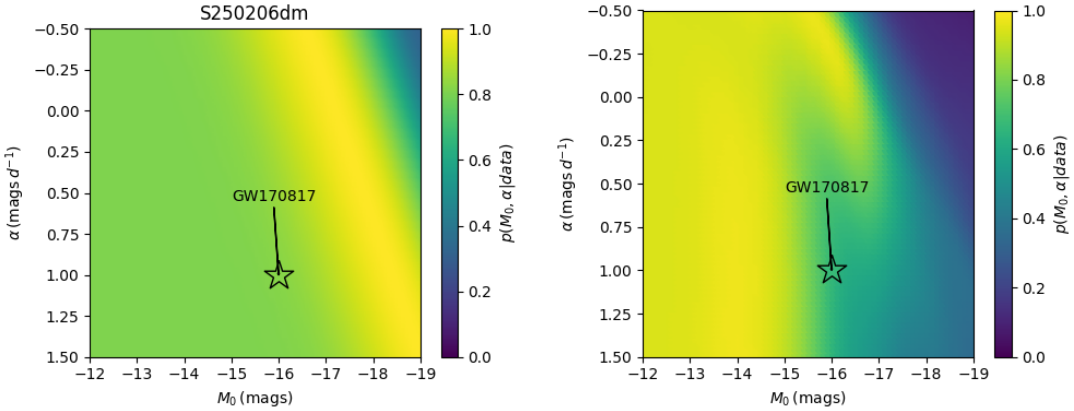

Figure 3. The `nimbus` results of (left) S250206dm and (right) the combined set of GW triggers: S250206dm, S230518h, S230627c, S230731an, S231113bw, GW200115, GW190524, GW190426, GW190814 and GW230529 for KN model parameters assuming the *Tophat* model. The *x*-axis shows the peak absolute magnitude M_0 of a model, while the y-axis shows its evolution rate α. The color bar shows the posterior probability of each model, where yellow regions show the favored regions of parameter space given the non-detection of KNe from ZTF observations, and the bluer regions show less preferred combinations for peak M_0 and α. We note that for S250602dm a GW170817-like KN is preferred at 82% level, while for the combined analysis it falls at the 67%.

S230518h, S230627c, S230731an, S231113bw, GW200115, GW190524, GW190426, GW190814 and GW230529.

Both `nimbus`, a Bayesian method, and `simsurvey`, a frequentist approach, provide independent but complementary insights into KNe from the ZTF observations. `simsurvey` assesses the recovery efficiency of KNe with specific model parameters in the ZTF follow-up, while `nimbus` helps identify which KN model parameters are more or less supported by the ZTF data. When comparing the results from both methods, we notice similar overall patterns. Rising or slowly decaying bright KNe ($M \lesssim -17.5$ mag and $\alpha < 0.25$) exhibit the highest efficiencies in `simsurvey`, as our simulation recovers these KNe with efficiencies up to 60%. The `nimbus` analysis evaluates whether a given KN model is favored by the ZTF non-detections. For S250206dm, `nimbus` disfavors a similar set of models ($P_{\texttt{nimbus}} < 0.4$ for $M \lesssim -17.5$ mag and $\alpha < 0.2$), as the ZTF data. In contrast, faint, fast-fading KNe have the lowest detection efficiencies in `simsurvey` and receive the most support from `nimbus` ($P_{\texttt{nimbus}} > 0.8$), based on the ZTF non-detections.

4.2. Ruling Out Merger Parameter Space

Here we use our photometric upper limits to constrain the parameter space for the compact binary merger. We simulate KN spectral models using the most recent version (Bulla 2023) of the 3D Monte Carlo radiative transfer code `possis` (Bulla 2019). Specifically, we present two new KN grids for BNS and NSBH mergers that are inspired by Anand et al. (2023) and Mathias et al. (2024), respectively, and use revised nuclear heating rates from Rosswog & Korobkin (2024). The two grids will be made publicly available at https://bit.ly/possis_models.

The BNS merger ejecta are described by two distinct axially symmetric components: a first component ejected on dynamical timescales (dynamical ejecta) and a second component ejected after the merger from a disk accreted around the merger remnant (post-merger disk-wind ejecta), see, e.g., Nakar (2020) for a review. Following Bulla (2023), a dependence on the polar angle θ is taken for both the density and the electron fraction in the dynamical ejecta ($\rho \propto \sin^2\theta$ and $Y_e \propto \cos^2\theta$), while spherical symmetry and uniform composition (i.e., fixed Y_e) are assumed for the wind ejecta (Perego et al. 2017; Radice et al. 2018; Setzer et al. 2023). The grid is controlled by six free ejecta parameters: dynamical mass $M_{\rm dyn} = (0.001, 0.005, 0.01, 0.02)\,M_\odot$, dynamical mass-weighted averaged velocity $\bar{v}_{\rm dyn} = (0.12, 0.15, 0.2, 0.25)$ c, dynamical mass-weighted averaged electron fraction $\bar{Y}_{\rm e,dyn} = (0.15, 0.20, 0.25, 0.30)$, wind mass $M_{\rm wind} = (0.01, 0.05, 0.09, 0.13)\,M_\odot$, wind mass-weighted averaged velocity $\bar{v}_{\rm wind} = (0.03, 0.05, 0.10, 0.15)$ c, and wind electron fraction $Y_{\rm e,wind} = (0.20, 0.30, 0.40)$. The number of models is 3072, which leads to a total number of KNe of 33 792 when accounting for the 11 different viewing angles $\theta_{\rm obs}$. These angles, which are distinct from the polar angle θ used to describe the KN geometry, are equally spaced in $\cos\theta_{\rm obs}$ from a face-on (polar) to a edge-on (equatorial) view of the system.

Similarly, the NSBH merger ejecta are described by dynamical and disk-wind ejecta components. However, we follow Kawaguchi et al. (2020) and adopt a stronger angular dependence focusing the dynamical ejecta around the merger plane as expected from NSBH systems, $\rho \propto 1/\{1 + \exp[-20\,(\theta - 1.2)]\}$. In addition, the compositions are the same for all the models in the grid and set to $Y_e = 0.1$ in the dynamical ejecta and $0.2 < Y_e < 0.3$ in the wind ejecta (Kawaguchi et al. 2020; Mathias et al. 2024). The NSBH KN grid is constructed using

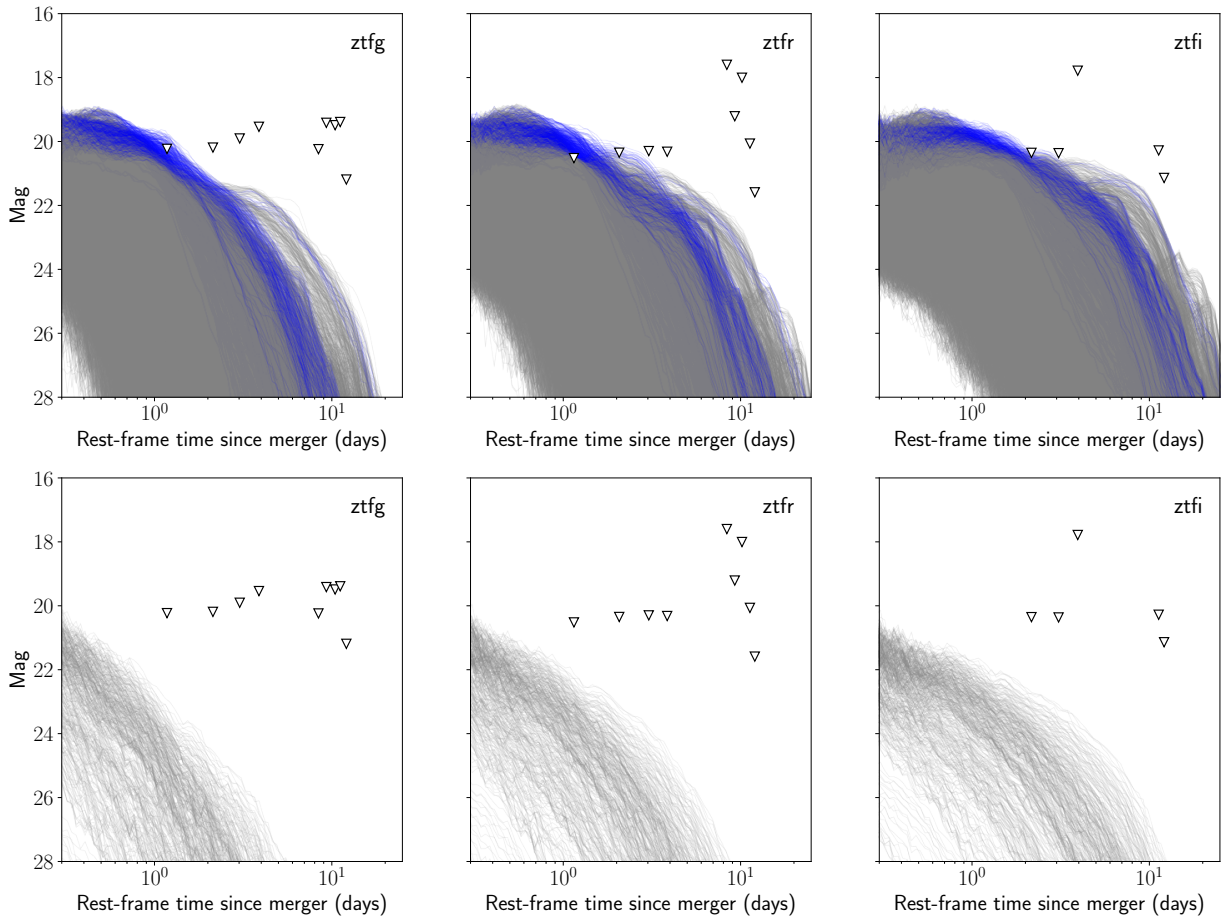

Figure 4. Light-curves of (top) BNS and (bottom) NSBH models, derived using the most recent version of `possis` (Bulla 2023), and pinned at 269 Mpc (gray), the closest 1σ from the GW distance distribution. We show the ZTF median limits as triangles for (left) *g*-band, (middle) *r*-band, and (right) *i*-band. A number of BNS models were ruled out (in blue), mostly due to the limits achieved during the first night of observations. No NSBH models were ruled out with the ZTF observations. These models are derived using the latest POSSIS, and the parameters for the BNS and NSBH grid are shown in Section 4.2.

binary properties and different equations of state (EoS) as free parameters. In particular, the neutron star mass $M_{\rm NS} = (1.2, 1.4, 1.6, 1.8)\,M_\odot$, black hole mass $M_{\rm BH} = (4.0, 6.0, 8.0)\,M_\odot$ and black hole spin $\chi_{\rm BH} = (0.0, 0.3, 0.6)$ are varied within the grid, while the DD2 (Hempel & Schaffner-Bielich 2010), the AP3 (Akmal et al. 1998) and the SFHo+HΔ (Drago et al. 2014) are chosen as possible EoSs. Ejecta masses and velocities are computed for each model using fitting formulae as described in Mathias et al. (2024), with 37 combinations of the free parameters that lead to the ejection of some material and therefore produce a KN (see their table 2). When accounting for the 11 different viewing angles, a total of 407 KNe are produced in this grid.

Figure 4 shows comparison between the ZTF upper limits and KN models from the adopted BNS (top row) and NSBH (bottom row) grids in *g* (left), *r* (middle) and *i* (right) filters. The distance is optimistically assumed to be at the closest 1σ end of the distribution provided by LVK, i.e., 269 Mpc. Even at this distance, no NSBH model can be ruled out as the resulting KNe are fainter than the upper limits in all filters. In contrast, some KN lightcurves from the BNS grid are brighter than the ZTF limits and are thus ruled out assuming the KN site was imaged during these observations. As shown in this figure, the most constraining data are those from the first observation ∼1.2 days after the LVK trigger and, particularly, from the *r* filter at ∼20.5 mag.

Figure 5 shows what regions of the ejecta parameter space are disfavored by our limits, assuming a face-on view of the system. Although no combination of the six ejecta parameters can be completely ruled out, we find that some combinations are clearly disfavored. For instance, high values for the wind ejecta mass and electron fraction are disfavored as they lead to bright KNe. The ZTF upper limits allow to rule out 35% of these models. We note that models with different viewing angles than face-on, are less constrained in general (see Appendix G).

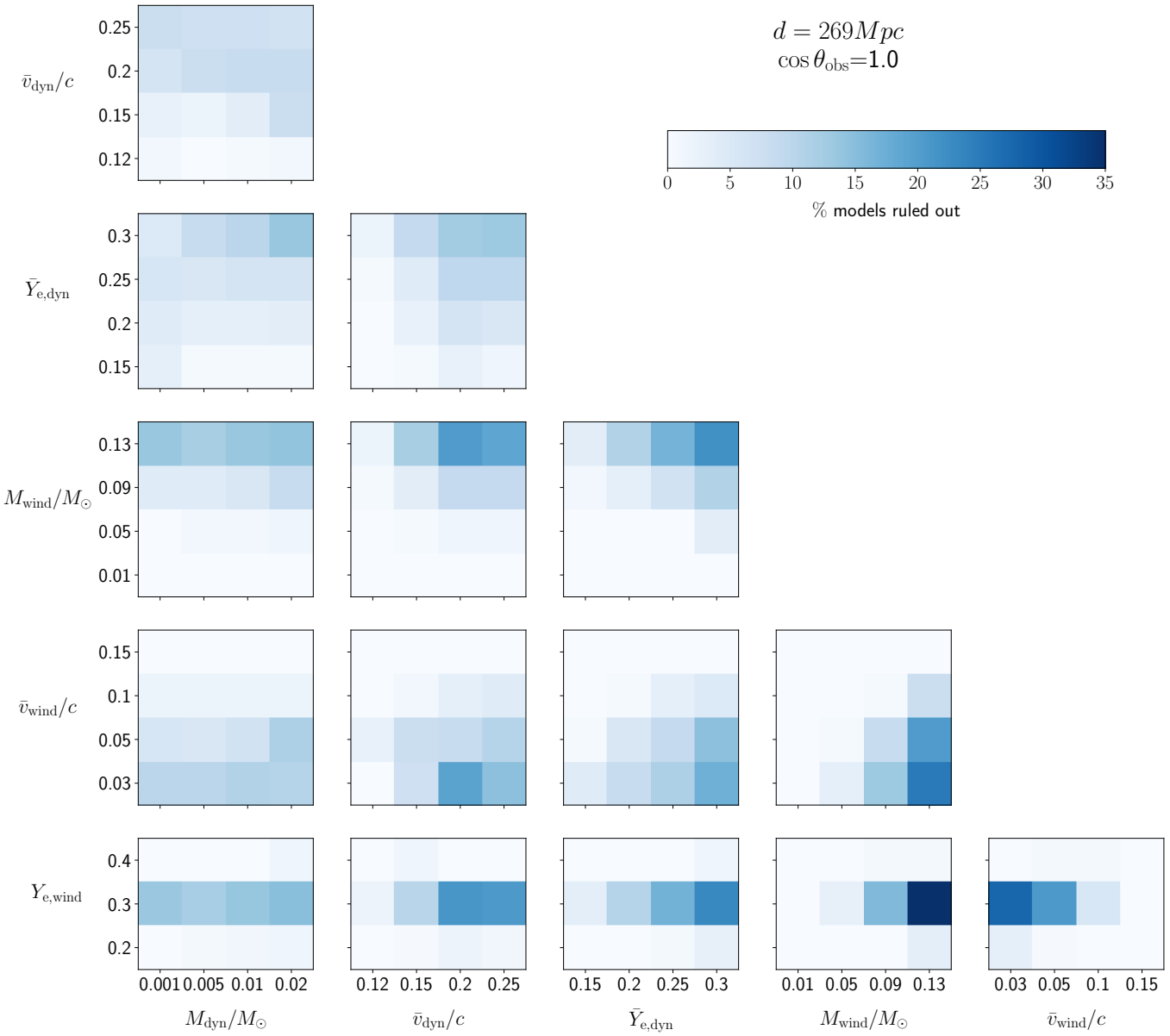

Figure 5. Corner plot showing in a colorbar the percentage of BNS models ruled out at a fixed distance of 269 Mpc and at a fixed viewing angle of 0 deg. The parameters correspond to the ejecta mass, mass-weighted averaged velocity and mass-weighted electron fraction for the dynamical and wind ejecta: $m_{\rm dyn}$, $\bar{v}_{\rm dyn}$, $\bar{Y}_{\rm e,dyn}$, $m_{\rm wind}$, $\bar{v}_{\rm wind}$ and $Y_{\rm e,wind}$.

5. Joint ZTF and DECam Observations

The region of S250206dm was targeted by numerous instruments, both in the northern and southern hemispheres. In the south, the GW-MMADS survey was able to cover close to 9.3% of the localization region with the Dark Energy Camera (DECam; Hu et al. 2025). In this section we combine the observation of ZTF and DECam to explore the efficiencies and determine how these instruments complement the GW searches. Together, these instruments covered 73.3% of the GW error region.

As described in Hu et al. (2025), DECam started observations of the GW skymap six days after the GW event and ran for several days, reaching on average 23 mag in the *r* band (see Figure 7). To assess the joint efficiency of using ZTF and DECam synoptic searches, we use `simsurvey`. Similarly to the ZTF only case, we simulate KNe in the GW skymap and feed `simsurvey` the observing logs of ZTF and DECam. The KNe are simulated independent of the observing logs and only their recovery rate depends on the executed observations. The DECam observations, although later in time, reach depths

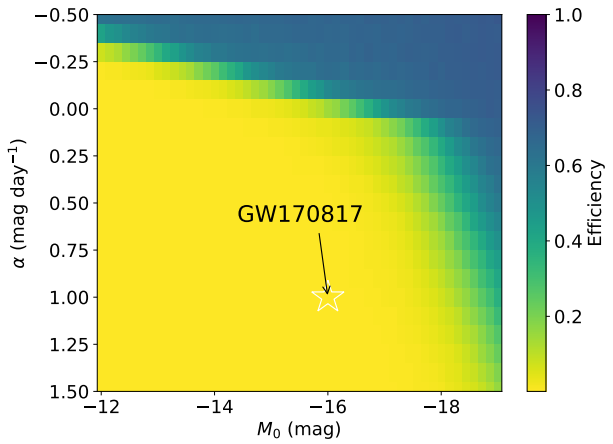

Figure 6. `simsurvey` recovery efficiency for KNe injected in the S250206dm skymap using a grid of peak absolute magnitude, M_0, and evolution rate, α, using ZTF and DECam observations. One of the main differences is that compared to the ZTF only analysis, the joint observations are more efficient at recovering fainter KN that have a slowly rising behavior ($\alpha < 0$).

comparable to the KN models. These, combined with the ZTF shallower limits from the first few nights, result in a higher combined efficiency at ruling out KNe (<-15 mag) that rise ($\alpha < 0$ mag day^{-1}) and bright KNe (<-16.5 mag) fading slowly ($\alpha < 0.3$ mag day^{-1}). For these cases, the combined efficiency for any KN (from a BNS or NSBH merger) is close to 60% (see Figure 6). The efficiency drops to levels similar to the ZTF-only analysis for KNe in the 170817-like parameter space, i.e., efficiency of $\approx$1% for $M_0 \approx -16$ mag and $\alpha = 1$ mag day^{-1}.

The `simsurvey` approach accounts for the fact that the two instruments cover different areas of the sky and reach different depths. In addition to this analysis, we present constraints in the KN model parameter space using the ZTF and DECam limits in tandem. Although this approach assumes joint coverage, which is not the case for S250206dm, we note that for future (and past) events, large-field-of-view instruments are expected to overlap in coverage. In such cases, joint analysis will be possible. In Figure 7, we show the *r*- and *i*-band limits of both ZTF and DECam for S250206dm. Under this assumption, the models ruled out by the joint set of upper limits reach 55% for face-on models with $M_{\rm wind} \approx 0.13\,M_\odot$ and $v_{\rm wind} \approx 0.03c$.

6. Conclusion

We used ZTF to conduct an optical search for the electromagnetic counterpart of the compact binary merger S250206dm. The GW event had a FAR of 1 in 25 yr, a 35% probability of being a BNS, and a 55% probability of being an NSBH if astrophysical. In either case, and if astrophysical in origin, the probability of having an NS involved is of 100%, whereas the probability of having a remnant that could power EM emission is 30%.

Due to poor weather during the first night, ZTF only began to observe the region 29 hr after the GW event. We tiled 68% of the region, and observed more than 470 sq deg of the latest error region.[33] ZTF returned to the region daily for nine days, using a mix of deep, targeted observations and shallower, serendipitous ones from its nominal public survey. We used Fritz, `emgwcave`, `nuztf`, and ZTFReST to filter the ZTF stream of alert and found 13 compelling candidates. All these ZTF candidates were ruled out as either spectroscopically or photometrically inconsistent with a KN, located outside of the GW volume, or associated with stellar sources. We analyzed candidates circulated through TNS, and with our follow-up we were able to rule out all but seven candidates. Assuming no KN was found, we derived the efficiency of the ZTF searches. Using a Bayesian approach, `nimbus`, we look for the probability of a KN to be in the ZTF data, and we find that our searches can rule out the presence of KNe with $M_0 < -17.5$ for S250206dm ($P_{\rm nimbus} < 0.4$), while our frequentist approach, `simsurvey`, we inject KN in the GW skymaps and derived the number of KN retrieved with ZTF, and this shows that ZTF is more efficient at finding KNe in the brighter end ($\sim$60% efficiency for KN with $M_0 < -17.5$). When analyzing all the ZTF GW follow-up combined, the addition of S250602dm only improves the efficiency of retrieving KNe on the brighter side of the parameter space. These results slightly improve the efficiencies reported in Ahumada et al. (2024), by 5% in the KN parameter space where $M_0 < -17.5$ mag and $\alpha < 1$ mag day^{-1}.

Assuming the KN is in the ZTF footprint, we compared our survey upper limits to KN models generated using the latest version of the 3D Monte Carlo radiative transfer code `possis`. We present two new model grids: one for BNS mergers and another for NSBH mergers, incorporating updated ejecta properties and nuclear heating rates. The BNS grid includes 3072 models spanning a range of six ejecta parameters and 11 viewing angles, while the NSBH grid comprises 407 models built from 37 parameter combinations based on different binary properties and equations of state. By comparing these models to ZTF upper limits in the *g*, *r*, and *i* bands, we find that none of the NSBH models are bright enough to be ruled out, whereas some BNS models exceed the observed limits and are therefore disfavored, especially those with higher wind mass and electron fraction. The most constraining observation occurred 1.2 days post-merger in the *r* band, reaching $\sim$20.5 mag. Overall, while no single combination of BNS parameters can be entirely excluded, our results disfavor certain regions of parameter space, particularly for face-on viewing angles.

[33] https://gracedb.ligo.org/api/superevents/S250206dm/files/Bilby.offline1.multiorder.fits

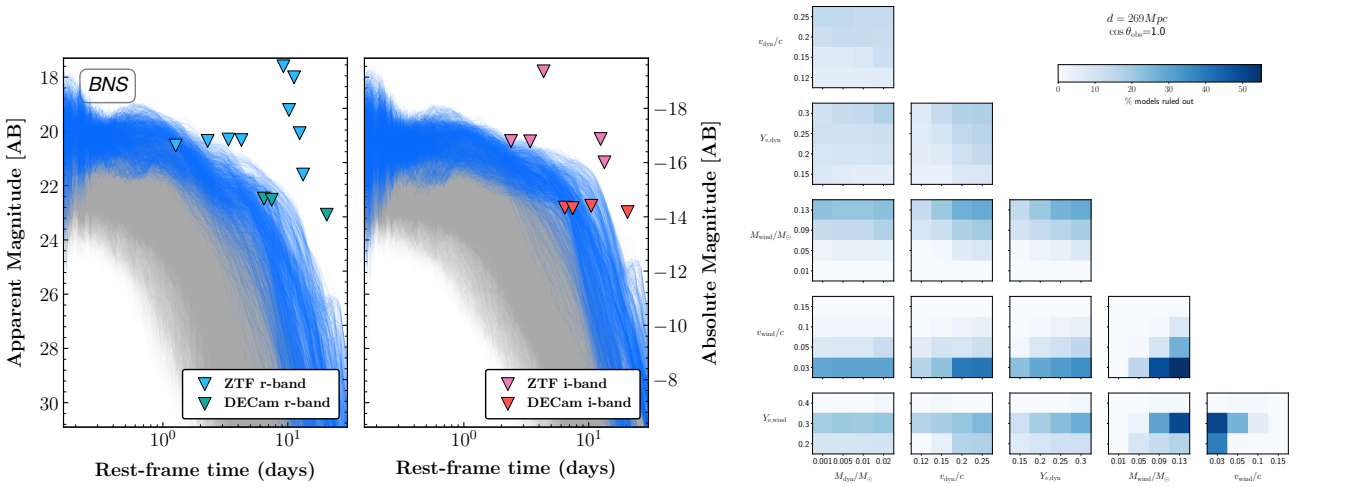

Figure 7. (left) Light-curves of BNS models pinned at 269 Mpc, the closest 1σ from the GW distance distribution. We show the ZTF and DECam median limits as triangles for (left) *r* band and (center) *i* band. BNS models were ruled out by both ZTF and DECam at different stages in the lightcuve. (right) Similar to Figure 5, we display a corner plot showing in a colorbar the percentage of BNS models ruled out at a fixed distance of 269 Mpc and at a fixed viewing angle of 0 deg. The maximum number of models ruled out goes up to 55% using the DECam and ZTF observations combined.

Finally, we performed a joint analysis of the ZTF and GW-MMADS DECam observations from (Hu et al. 2025) of S250206dm to assess their combined efficiency in detecting KNe. ZTF began imaging earlier than DECam, although it provided shallower limits compared to DECam ($\sim$23 mag in the *r* band). Using the `simsurvey` framework, we simulated KNe across the GW skymap and evaluated recovery efficiencies based on the actual observing logs from both instruments. The joint data set improves efficiency in detecting faint, slowly rising KNe (with $\alpha < 0$ mag day^{-1}) and bright, slowly fading KNe (with $\alpha > 0.3$ mag day^{-1}), reaching up to 60% recovery in those regimes, significantly better than ZTF alone. Although DECam and ZTF covered different regions for this event, we also explored constraints assuming overlap in coverage, finding that up to 55% of BNS models could be ruled out at 269 Mpc, particularly those with high wind mass and low wind velocity. These results highlight the value of combining wide-field optical data sets for future joint GW-KN searches, while also emphasizing that both early observations and deep, late observations since the GW event could help strongly constrain the KN parameter space.

Acknowledgments

M.M.K., S.A. and T.A. acknowledge generous support from the David and Lucile Packard Foundation. M.B. acknowledges the Department of Physics and Earth Science of the University of Ferrara for the financial support through the FIRD 2024 grant M.W.C., A.T., A.S. and T.B. acknowledges support from the National Science Foundation with grant No. PHY-2010970. A.T. acknowledges support from the National Science Foundation with grant Nos. PHY-2308862 and PHY-2117997 A.P. and L.H. acknowledges support by National Science Foundation grant No. 2308193. I.A. acknowledges support from the National Science Foundation Award AST 2505775 and NASA grant 24-ADAP24-0159 A. S.ngh acknowledges support from the Knut and Alice Wallenberg Foundation through the "Gravity Meets Light" project. C.M.C. acknowledges support from UKRI with grant numbers ST/X005933/1 and ST/W001934/1 A. S. acknowledges support from the National Science Foundation with grant number PHY-2010970. M.B. is supported by a Student Grant from the Wübben Stiftung Wissenschaft. G.C.A. thanks the Indian National Science Academy for support under the INSA Senior Scientist Programme. A.T. acknowledges support from the National Science Foundation with grant Nos. PHY-2308862 and PHY-2117997.

Based on observations obtained with the Samuel Oschin Telescope 48 inch and the 60 inch Telescope at the Palomar Observatory as part of the Zwicky Transient Facility project. ZTF is supported by the National Science Foundation under grants Nos. AST-1440341, AST-2034437, and currently Award #2407588. ZTF receives additional funding from the ZTF partnership. Current members include Caltech, USA; Caltech/IPAC, USA; University of Maryland, USA; University of California, Berkeley, USA; University of Wisconsin at Milwaukee, USA; Cornell University, USA; Drexel University, USA; University of North Carolina at Chapel Hill, USA; Institute of Science and Technology, Austria; National Central University, Taiwan, and OKC, University of Stockholm, Sweden. Operations are conducted by Caltech's Optical Observatory (COO), Caltech/IPAC, and the University of Washington at Seattle, USA.

SED Machine is based upon work supported by the National Science Foundation under grant No. 1106171.

The ZTF forced-photometry service was funded under the Heising-Simons Foundation grant #12540303 (PI: Graham).

The Gordon and Betty Moore Foundation, through both the Data-Driven Investigator Program and a dedicated grant, which provided critical funding for SkyPortal.

We acknowledge the support from the National Science Foundation GROWTH PIRE grant No. 1545949.

This work used Expanse at the San Diego Supercomputer Cluster through allocation AST200029—"Towards a complete catalog of variable sources to support efficient searches for compact binary mergers and their products" from the Advanced Cyberinfrastructure Coordination Ecosystem: Services & Support (ACCESS) program, which is supported by National Science Foundation grants #2138259, #2138286, #2138307, #2137603, and #2138296. This research has made use of the NASA/IPAC Extragalactic Database (NED), which is funded by the National Aeronautics and Space Administration and operated by the California Institute of Technology.

The Liverpool Telescope is operated on the island of La Palma by Liverpool John Moores University in the Spanish Observatorio del Roque de los Muchachos of the Instituto de Astrofisica de Canarias with financial support from the UK Science and Technology Facilities Council.

This work relied on the use of HTCondor via the IGWN Computing Grid hosted at the LIGO Caltech computing clusters.

Some of the data presented herein were obtained at Keck Observatory, which is a private 501(c)3 non-profit organization operated as a scientific partnership among the California Institute of Technology, the University of California, and the National Aeronautics and Space Administration. The Observatory was made possible by the generous financial support of the W.M. Keck Foundation. The authors wish to recognize and acknowledge the very significant cultural role and reverence that the summit of Maunakea has always had within the Native Hawaiian community. We are most fortunate to have the opportunity to conduct observations from this mountain.

The GROWTH India Telescope (GIT) is a 70 cm telescope with a $0.^{\circ}7$ field of view, set up by the Indian Institute of Astrophysics (IIA) and the Indian Institute of Technology Bombay (IITB) with funding from DST-SERB and IUSSTF. It is located at the Indian Astronomical Observatory (Hanle), operated by IIA. We acknowledge funding by the IITB alumni batch of 1994, which partially supports the operations of the telescope. Telescope technical details are available at https://sites.google.com/view/growthindia/.

This paper contains data obtained at the Wendelstein Observatory of the Ludwig-Maximilians University Munich. We thank Christoph Ries and Michael Schmidt for obtaining the observations. Funded in part by the Deutsche Forschungsgemeinschaft (DFG, German Research Foundation) under Germany's Excellence Strategy—EXC-2094—390783311.

Appendix A
ZTF Coverage of Multi-wavelength and Multi-messenger Candidates

In this section, we zoom in on the localization associated with the radio and neutrino sources and show the associated ZTF coverage (see Figure 8).

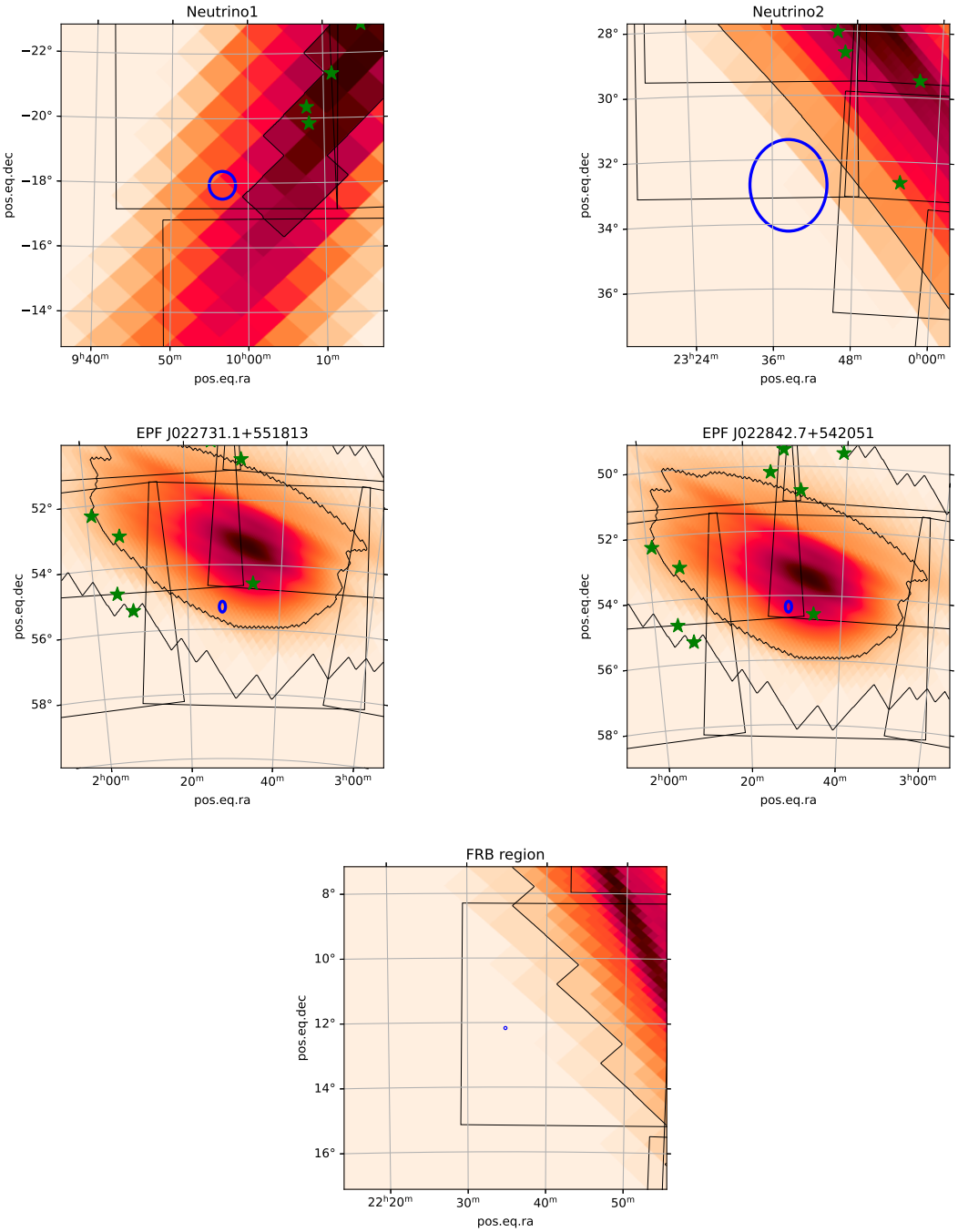

Figure 8. Localization of the high-significance event S250206dm, overlaid with the ZTF tiles and the 90% probability contour. The blue region shows the center of different multi-wavelength and multi-messenger transients detected coincident in time with S250206dm. The green stars represent the transients circulated on TNS, accessible from Palomar.

Appendix B
Follow-up Details

B.1. Photometric Follow-up

Palomar 60 inch. We acquired photometric data utilizing the Spectral Energy Distribution Machine (SEDM; Blagorodnova et al. 2018; Rigault et al. 2019; Kim et al. 2022) mounted on the Palomar 60 inch telescope. The SEDM is a low resolution ($R \sim 100$) integral field unit spectrometer with a multi- band (*ugri*) Rainbow Camera (RC). The follow-up request process is automated and can be initiated through `Fritz`. Standard requests typically involved 180 s exposures in the *g*-, *r*-, and *i*-bands, however, it can be customized and for some transients we used 300 s exposures. The data

undergoes reduction using a Python-based pipeline, which applies standard reduction techniques and incorporates a customized version of FPipe (Fremling Automated Pipeline; Fremling et al. 2016) for image subtraction.

GROWTH-India Telescope. We utilized the 0.7 m robotic GROWTH-India Telescope (GIT; Kumar et al. 2022), located in Hanle, Ladakh. It is equipped with a 4k back-illuminated camera that results in a 0.82 deg^2 field of view. Data reduction is performed in real-time using the automated GIT pipeline. Photometric zero points were determined using the PanSTARRS catalogue, and PSF photometry was conducted with PSFEx (Bertin & Arnouts 2010). In cases where sources exhibited a significant host background, we performed image subtraction using `pyzogy` (Guevel & Hosseinzadeh 2017), based on the ZOGY algorithm (Zackay et al. 2016).

Liverpool Telescope. The images acquired with the Liverpool Telescope (LT) were taken using the IO:O (Steele et al. 2004) camera equipped with the Sloan *griz* filterset. These images underwent reduction through an automated pipeline, including bias subtraction, trimming of overscan regions, and flat fielding. Image subtraction occurred after aligning with a PanSTARRS template, and the final data resulted from the analysis of the subtracted image.

Fraunhofer Telescope at Wendelstein Observatory. We conducted follow-up observations using the Three Channel Imager (3KK; Lang-Bardl et al. 2016) on the 2.1 m Fraunhofer Telescope at Wendelstein Observatory (FTW; Hopp et al. 2014), located on Mt. Wendelstein at the northern edge of the Alps. The 3KK imager enables simultaneous imaging in three channels. For our observations, we configured the blue, red, and near-infrared channels with the *r*, *i*, and *J* bands, respectively. We applied standard data reduction techniques to derive magnitudes for the follow-up. For details on the 3KK data reduction see Busmann et al. 2025b and Gössl & Riffeser 2002.

B.2. Spectroscopic Follow-up

Keck I. We obtained spectra with LRIS on the Keck I telescope, using the 600/4000 grism on the blue side and the 600/7500 grating on the red side. This setup provided wavelength coverage from 3139–5642 Å in the blue and 6236–9516 Å in the red. Both arms were exposed for 600 s. The data were reduced using LPipe (Perley 2019), with BD+28 serving as the flux calibrator. To ensure accurate relative flux calibration between the red and blue sides, we scaled the spectra by matching synthetic photometry to observed transient colors.

Palomar 200 inch. We observed ZTF candidates using the Palomar 200 inch Next Generation Palomar Spectrograph (NGPS). The setup configuration used a 1.″5 slitmask, a D55 dichroic, a blue grating of 600/4000, and a red grating of 316/7500. We applied a custom PyRAF DBSP reduction pipeline (Bellm & Sesar 2016) to process and reduce our data.

Nordic Optical Telescope. We obtained spectra of potential candidates and their host galaxies using the Alhambra Faint Object Spectrograph and Camera (ALFOSC) mounted on the Nordic Optical Telescope. We used Grism #4 with a 1″ slit. The spectra were reduced in a standard manner using a custom fork of `PypeIt` (Prochaska et al. 2020b, 2020a, 2020c).

Appendix C
Candidate Analysis

In this section, we describe the candidates found in the 95% region of S250206dm, as well as the reasons to rule them out. Comparing the sources found by other surveys with those detected by ZTF helps refine our strategy for candidate selection and source filtering (see Tables 1–3 and Figures 9–11).

Table 1
Candidates from ZTF

Team	AT Name	R.A. (deg)	Decl. (deg)	Δt (days after GW)	Discovery mag. (AB magnitude)	C.R.	Redshift	Rejection Criterion
ZTF	AT2025bcq	36.312650	50.177961	2.36	$g = 20.38$ mag	0.57	⋯	stellar
ZTF	AT2025bda	354.338535	22.979038	1.23	$g = 19.92$ mag	0.66	$z_{ph} = 0.789$	slow evolution
ZTF	AT2025bay	7.504874	37.168325	1.24	$r = 20.51$ mag	0.69	$z_{spec} = 0.19$	SN Ia
ZTF	AT2025brm	359.267230	29.487675	4.23	$g = 20.41$ mag	0.73	⋯	old
ZTF	AT2025ben	356.321031	28.022989	3.22	$r = 19.44$ mag	0.76	$z_{ph} = 0.074$	slow evolution
ZTF	AT2025bro	356.597145	28.657444	1.21	$r = 20.08$ mag	0.77	$z_{ph} = 0.146$	slow evolution
ZTF	AT2025brn	2.037106	32.845540	4.23	$g = 20.34$ mag	0.79	⋯	slow evolution
ZTF	AT2025bcx	7.352266	38.690377	1.24	$r = 20.75$ mag	0.81	⋯	slow evolution
ZTF	AT2025bcw	21.331975	45.271967	1.25	$r = 20.67$ mag	0.84	⋯	old
ZTF	AT2025brp	358.691917	32.650467	1.22	$r = 20.50$ mag	0.87	$z_{ph} = 0.61$	slow evolution
ZTF	AT2025brl	1.907439	27.964044	4.23	$g = 19.96$ mag	0.93	⋯	stellar
ZTF	AT2025bcr	20.491312	48.970425	2.28	$r = 20.59$ mag	0.93	⋯	slow evolution
ZTF	AT2025cdh	156.656672	−25.498773	11.51	$g = 19.16$ mag	0.95	⋯	slow evolution

Table 2
Candidates Circulated on TNS Accessible from Palomar

Team	AT Name	R.A. (deg)	Decl. (deg)	Δt	Discovery mag. (AB magnitude)	C.R.	Redshift	Rejection criterion
WL-GW	AT2025bmq	38.517583	54.572472	2.01	$i = 20.00$ mag	0.16	$z_{\rm ap} = 0.08$	old
Pan-STARRS	AT2025bew	31.571696	53.010387	1.42	$r = 20.86$ mag	0.44	⋯	slow evolution
Pan-STARRS	AT2025bev	30.246246	52.324672	1.41	$r = 21.35$ mag	0.51	⋯	slow evolution
Pan-STARRS	AT2025bbn	37.788441	50.735331	1.37	$r = 20.19$ mag	0.52	⋯	stellar
Pan-STARRS	AT2025bbm	36.962653	49.475908	1.37	$r = 20.03$ mag	0.72	⋯	stellar
SAGUARO	AT2025azm	2.031278	32.565750	0.31	Clear = 20.10 mag	0.77	$z_{\rm ph} = 0.074$	old
Pan-STARRS	AT2025bbo	24.321968	45.725504	1.39	$r = 20.05$ mag	0.86	⋯	artifact
SAGUARO	AT2025azn	39.822573	49.572528	0.31	Clear = 19.97 mag	0.87	$z_{\rm spec} = 0.35$	outside volume
Pan-STARRS	AT2025bex	24.462509	45.339600	3.35	$i = 20.80$ mag	0.88	⋯	rising LT
Pan-STARRS	AT2025bbt	45.469074	51.129734	1.42	$r = 18.64$ mag	0.88	⋯	old
GOTO	SN 2025bpv	156.224083	−27.081777	0.69	$L = 20.19$ mag	0.93	$z_{\rm spec} = 0.068$	SN Ia
Pan-STARRS	AT2025baw	153.431093	−24.613802	0.54	$r = 20.70$ mag	0.93	$z_{\rm ph} = 0.24$	old
Pan-STARRS	AT2025bai	151.935085	−20.342932	0.54	$r = 19.78$ mag	0.94	$z_{\rm ph} = 0.09$	old
Pan-STARRS	SN 2025bag	154.613735	−26.732906	0.52	$r = 17.51$ mag	0.94	$z_{\rm spec} = 0.03$	SN Ia
Candidates not ruled out								
Pan-STARRS	AT2025bcc	32.029016	55.342481	1.44	$r = 19.57$ mag	0.88	⋯	undefined
Pan-STARRS	AT2025bey	25.754872	45.463406	4.33	$z = 20.13$ mag	0.89	⋯	undefined
Pan-STARRS	AT2025bbp	153.782352	−22.881593	1.54	$r = 20.77$ mag	0.92	$z_{\rm ph} = 0.11$	likely outside volume
Pan-STARRS	AT2025bah	152.779896	−21.374558	0.53	$r = 18.69$ mag	0.92	$z_{\rm ph} = 0.15$	likely outside volume
Pan-STARRS	AT2025bam	152.008807	−19.840772	0.55	$r = 20.69$ mag	0.94	$z_{\rm ph} = 0.56$	likely outside volume
Pan-STARRS	AT2025bce	31.232391	54.795342	1.40	$r = 19.80$ mag	0.95	⋯	undefined
Pan-STARRS	AT2025baf	158.506625	−29.746992	0.52	$r = 19.33$ mag	0.95	$z_{\rm ph} = 0.64$	likely outside the volume

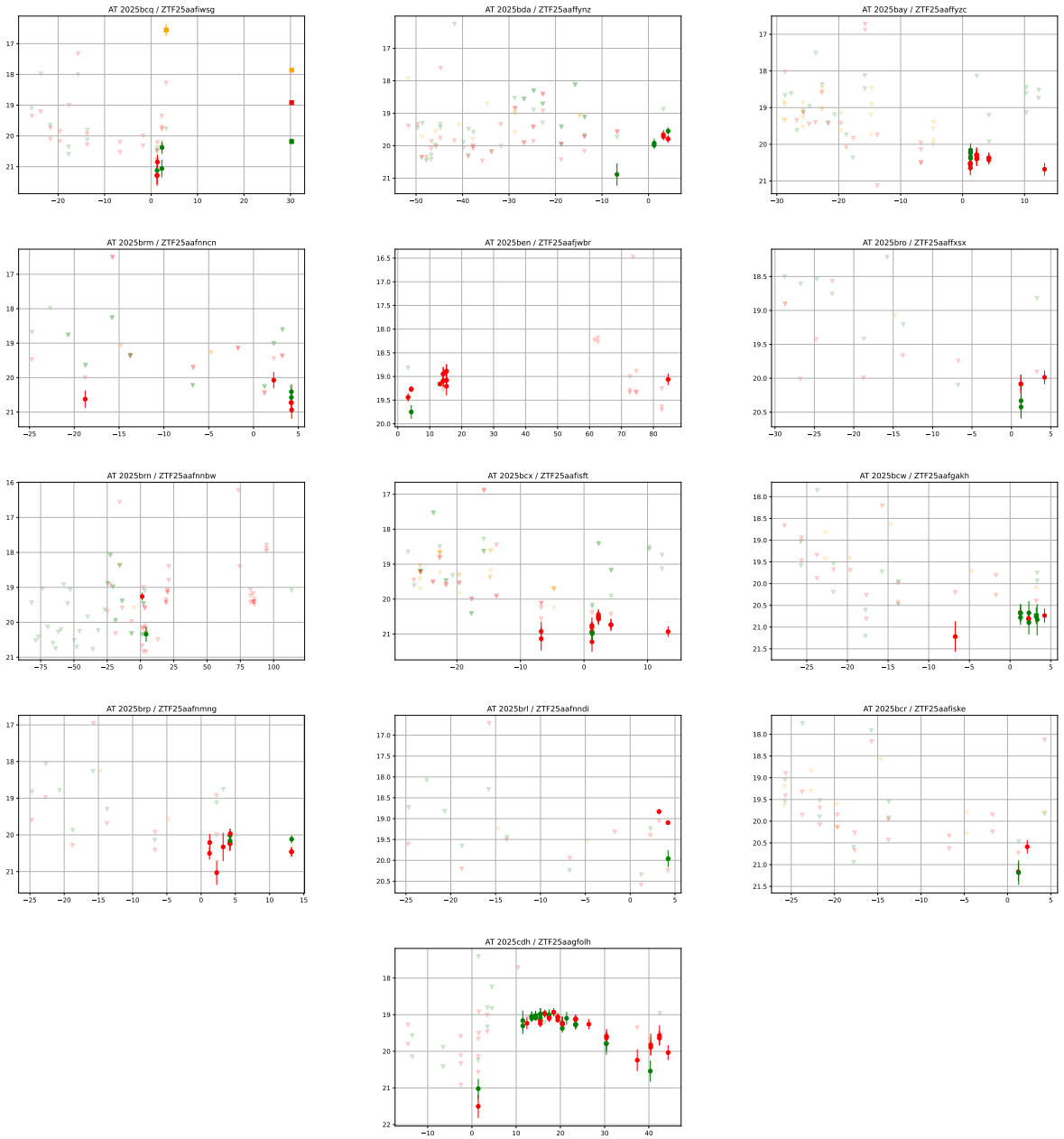

Figure 9. Light-curves for optical counterparts of S250206dm. The color (red, green, yellow, blue, cyan) represent the different filters (*g*, *r*, *i*, *L*, *c*). The different symbols (circle, square, pentagon, diamond, X, filled cross, and thin cross) represent the different facilities (ZTF, SEDM, PS1, LT, GIT, GOTO, CSS).

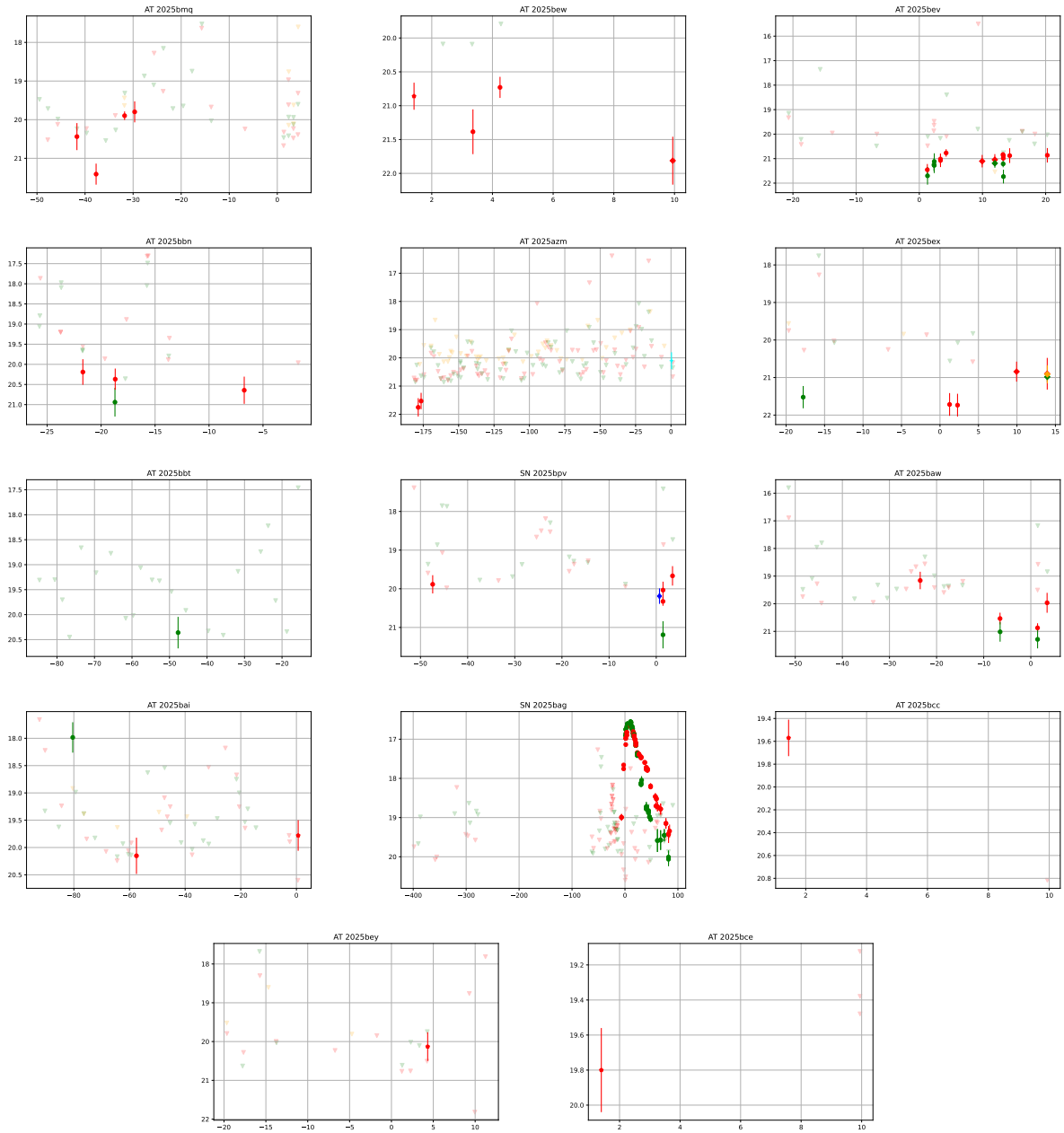

Figure 10. Light-curves for optical counterparts of S250206dm. The color (red, green, yellow, blue, cyan) represent the different filters (g, r, i, L, c). The different symbols (circle, square, pentagon, diamond, X, filled cross, and thin cross) represent the different facilities (ZTF, SEDM, PS1, LT, GIT, GOTO, CSS).

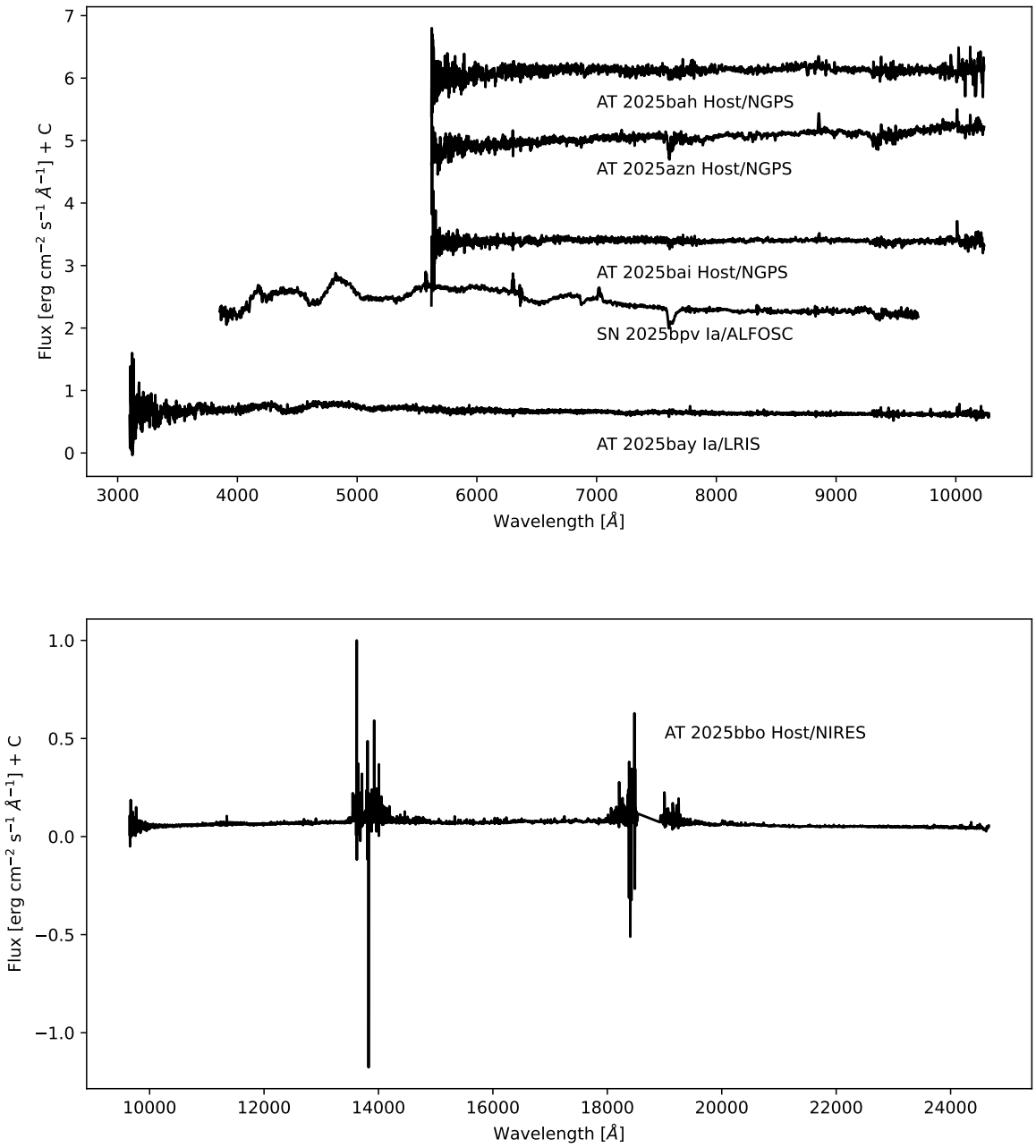

Figure 11. The optical (top) and near-infrared (bottom) spectra of the counterpart candidates of S250602dm.

C.1. Candidates Found with ZTF

AT2025bcq. Originally found as ZTF25aafiwsg, this transient was discovered at $g = 20.38$ mag, 2.3 days after the GW alert. The source is consistent with a star in the Gaia DR3 (Gaia Collaboration et al. 2023) within 2″. We ruled it out as it is a stellar source.

AT2025bda. Discovered as ZTF25aaffynz, this transient was at $g = 20.88$ mag and rose to $g = 19.5$ mag in 11 days. We ruled it out due to its slow evolution. We note the potential host galaxy has a photometric redshift of $z_{ph} = 0.789$ based on the Legacy Survey measurements.

AT2025bay. Discovered as ZTF25aaffyzc, at $r = 20.51$ mag 1.2 days after the trigger, we conducted prompt spectroscopic observations with Keck I/LRIS to classify it as a Type Ia SN at $z_{\rm spec} = 0.19$ Karambelkar et al. (2025a). Additionally, the source showed a slow evolution in the r band, inconsistent with a KN.

AT2025brm. Originally identified as ZTF25aafnncn, this source was discovered at $g = 20.41$ mag and 4.2 days after the merger. The source is next to a stellar source and forced photometry in the ZTF data shows a 4.5σ detection 30 days before the merger, which we interpret as previous activity. We rule it out as an old, unrelated source.

AT2025ben. ZTF25aafjwbr was discovered at $r = 19.44$ mag and 17 hr after the merger. It is located in the nucleus of the elliptical galaxy WISEA J234517.01+280121.7. The source slowly rose to a peak of $r = 18.8$ mag in 3 days, thus we ruled it out based on the slow photometric evolution.

AT2025bro. Detected as ZTF25aaffxsx at $r = 20.08$ mag, this source is in the outskirts of a galaxy with photometric redshift of $z_{\rm phot} = 0.146$. This puts the transient potentially outside of the GW volume of interest. Additionally, photometric monitoring of the source showed no evolution in the first 3 days after discovery in the r band, thus we ruled out this source based on its slow evolution.

AT2025brn. First discovered as ZTF25aafnnbw, this transient is hostless and the first detection was 4 days after the GW event and the candidate passed our filters as there was a forced photometry detection on day 2 at $r = 19.2$ mag. We rule out this source due to its slow evolution.

AT2025bcx. Detected with ZTF as ZTF25aafisft at $r = 20.9$ mag 1.2 days after the GW event, it remained active without evolving. We rule it out due to its slow evolution.

AT2025bcw—Discovered as ZTF25aafgakh at $r = 20.67$ mag, this source is 1″ from a red, point source. Forced photometry from ZTF revealed activity during the 50 days prior to the GW event, and the continuous monitoring with ZTF and LT did not show any evolution. Thus we reject this source as both old and not evolving.

AT2025brp. Originally as ZTF25aafnmng, it was detected 1.2 days after the GW event at $r = 20.5$ mag. The source is in the outskirts of an elliptical galaxy with LS photometric redshift of $z_{\rm phot} = 0.61$, potentially placing it outside of the GW volume. The continuous monitoring with ZTF showed no evolution in 12 days. Thus we reject it due to its lack of evolution.

AT2025brl. Initially discovered 4 days after the GW event, ZTF25aafnndi showed 2 previous detections (forced photometry) 2 days after the GW event. After further inspection, the source is classified as stellar activity due to its proximity (1.″9) to a star with $g = 15.7$ mag.

AT2025bcr. Initially detected as ZTF25aafiske, this source is located between a galaxy and a point source. Monitoring with the LT showed no evolution over a period of four days, thus ruling it out.

AT2025cdh. Originally ZTF25aagfolh, this source has shown a photometric evolution similar to a supernova, rising from $g = 21$ mag to $g = 19$ mag in 15 days and showing a slow decay. We therefore ruled it out due to its slow evolution.

C.2. Follow-up of Candidates from other Facilities

To determine whether each candidate is associated with the GW event, we apply the same rejection criteria used for ZTF sources: forced photometry of in ZTF images, cross-match to different catalogs, photometric and spectroscopic follow-up with ZTF and partner facilites. For each candidate, we describe the observations that led to its rejection.

AT2025bmq. Originally detected by us, this source is associated with WISEA J023404.21+543420.9, at a redshift of 0.08. Forced photometry of ZTF revealed an active source with bursts between 45 and 10 days before the GW trigger. Our FTW data showed a $r = 20.03$ mag source 11 days after the merger. Thus we ruled out this candidate as old with respect to the GW trigger, and due to its slow evolution.

AT2025bew. Discovered by Pan-STARRS at $i = 20.86$ mag, this source showed no significant evolution in our FTW and LT images, as it was detected at $i = 21.6$ mag after 10 days. We rule out this candidate due to its slow evolution rate of 0.07 mag day^{-1}.

AT2025bev. This source was discovered by Pan-STARRS, and also detected in the ZTF stream. The monitoring with ZTF, FTW and LT showed a slowly rising source that peaked at $r = 20.7$ mag 5 days after the GW event, and slowly decayed at a 0.03 mag day^{-1} rate. We ruled out this source based on its slow evolution.

AT2025bbn. Originally discovered by Pan-STARRS, the source is coincident with a point source we classified as a star using Gaia data. Additionally, ZTF forced photometry shows previous activity starting 30 days prior to the GW event.

AT2025bbm. Similarly, this source was announced by Pan-STARRS, and has a match to a stellar source in the Gaia database.

AT2025bbo. Detected by Pan-STARRS, this nuclear source associated with WISEA J013717.29+454331.9, with a

photometric redshift of 0.062. The monitoring with LT showed no evolution 4 days after the Pan-STARRS detection. We acquired a spectrum with NIRES, which showed only emission lines at a common redshift of 0.07 (Karambelkar et al. 2025b), the redshift of the host. This candidate was later retracted as an artifact (Huber et al. 2025a).

AT2025bex. Discovered by Pan-STARRS, this source is coincident with a point source with $B = 21.98$ mag. ZTF forced photometry shows a g-band detection 17 days before the GW event. Additionally, the monitoring with FTW and LT showed a rising source 10 days after the GW event, inconsistent with a KN.

AT2025bbt. This source, originally detected by Pan-STARRS, has a ZTF forced photometry detection 45 days prior to the GW event.

SN 2025bpv. This source was originally detected by GOTO. Our NOT spectra showed SN-like features, and fit a SN Ia template at a redshift of 0.0688. This source appears as ZTF25aagacqk in the ZTF data stream.

AT2025baw. This source first discovered by Pan-STARRS is coincident with a galaxy with LS photometric redshift of 0.2495. It has multiple forced photometry detections in the ZTF data stream. We ruled out this source as old.

AT2025bai. This source was first detected by Pan-STARRS, near the nucleus of a spiral galaxy with LS photometric redshift of 0.0991. The source had multiple ZTF detections before the GW event.

SN 2025bag. This source was first detected by Pan-STARRS, and it was additionally detected by ZTF as ZTF25aafhecq. The source has been classified as a SN Ia, and has a lightcurve extending for over 60 days.

AT2025azm. This source was first detected by SAGUARO, in the nucleus of a galaxy with LS photometric redshift of 0.07. This source has ZTF forced photometry detections that indicate this source was active 150 days before the GW event.

AT2025azn. This source was detected originally by SAGUARO, associated with WISEA J023917.49+493420.9, an elliptical galaxy at a photometric redshift of 0.0804. The NGPS spectrum of this galaxy shows lines at a common redshift of 0.35, placing the candidate outside of the GW volume.

AT2025bcc. This source was first detected by Pan-STARRS as a hostless transient. Our observations with FTW and LT do not show any sources down to a 5σ of $r > 23.5$ mag, $i > 23.1$ mag, and $J > 21.7$ AB, 4 days after the GW event. We cannot rule out this transient under any of our rejection criteria.

AT2025bey. This candidate was detected by Pan-STARRS in association with an elliptical galaxy. Our LT monitoring shows $r > 21.82$ mag, 4 days after the GW event. We cannot rule out this source under any of our rejection criteria.

AT2025baf. This source was detected by Pan-STARRS in association with a galaxy with a photometric redshift from LS of 0.6429, putting it outside the GW volume. We disfavor a GW association, though we note this conclusion is based solely on photometric redshift.

AT2025bah. This source was originally detected by Pan-STARRS, and coincident with a galaxy with an LS photometric redshift of 0.1586. This would put the transient outside the GW volume.

AT2025bbp. This source, discovered by Pan-STARRS, is associated to a galaxy with an LS photometric redshift of 0.1121, putting the target outside the volume of the GW event.

AT2025bam. Detected by Pan-STARRS, this source is coincident with a galaxy with a LS photometric redshift of 0.5661, putting the source outside of the GW volume.

AT2025bce. This transient was first detected by Pan-STARRS. Our LT observations 7 days after the merger found no transient up to a limiting magnitude of $r > 19.9$ mag. Similarly our FTW data showed no source down to limiting magnitudes of $r > 23.6$ mag, $i > 23.2$ mag, $J > 21.8$ AB mag.

Appendix D
Forecasts of Kilonova Lightcurves for ZTF Bands

We have developed a machine learning model using bidirectional long-short-term memory (LSTM) networks to forecast KN lightcurves based on low-latency alerts from IGWN, focusing on ZTF bands.

We use publicly available simulated observation data from the IGWN User Guide,[34] including 17,009 binary neutron star (BNS) and 3,148 neutron star black hole (NSBH) events[35] that exceed the IGWN detection threshold (SNR > 8) (Weizmann Kiendrebeogo et al. 2023). Sky maps are generated for simulated BNS and NSBH mergers using the Bayestar localization code (Singer & Price 2016), extracting parameters such as sky position, distance and the 90% localization area. Since the simulations provide only SNR, we map SNR to FAR using a large set of BNS injections to estimate $P_{\rm Astro}$.

We calculate probabilities from the EM-bright[36] classification, which estimates the likelihood that a merger involves at least one neutron star (HasNS), produces ejecta (HasRemnant), or includes a neutron star in the 3–5 solar mass range (HasMassGap).

Lastly, we use the NMMA[37] framework, which incorporates the POSSIS model (Bulla 2019; Dietrich et al. 2020), to generate lightcurves for each simulated compact binary coalescence.

We train a machine learning model to forecast KN lightcurves using features such as area (90%), distance, longitude, latitude, HasNS, HasRemnant, HasMassGap, and $P_{\rm Astro}$. To ensure consistency in scale and measurement units across the training data set, we apply the RobustScaler. The data is split into a 70/30 ratio for training and testing. In the

[34] https://emfollow.docs.ligo.org/userguide/capabilities.html
[35] https://zenodo.org/records/12696721
[36] https://git.ligo.org/emfollow/em-properties/em-bright
[37] https://nuclear-multimessenger-astronomy.github.io/nmma/fitting.html

test set, we achieve a mean squared error (MSE) of 0.24 in the g-band and 0.16 in the r-band.

For the 250206dm event, we collect the necessary features (FAR, area (90%), distance, longitude, latitude, HasNS, HasRemnant, HasMassGap, and $P_{\rm Astro}$) and use them to forecast the KN lightcurve with our machine learning model. This analysis was performed offline, after the manual vetting of the candidates was complete.

None of the candidates is consistent with our forecasts for the 250206dm event. The model's performance is further improved by integrating dynamical and wind ejecta as additional features, enhancing its ability to capture KN lightcurves, and significantly improving performance, reducing the MSE of 0.16 in the g-band and 0.11 in the r-band. However, even with these improvements, none of the candidates matched our predictions.

Appendix E
`nimbus` Framework

The notation is stated as follows:

1. $M^{\lambda}(t)$: The absolute magnitude in a given filter λ at a given time t.
2. M_0 : Initial absolute magnitude.
3. α : Evolution rate.
4. N_E : Total number of events that were followed up, indexed by i.
5. N_F : Total number of fields-of-view for which EM observations have been recorded, indexed by f.
6. N_f : Total number of observations for field f.
7. t_j^f : Time of observation, indexed by j for each field f over the duration of follow-up of the event. j would run over the total number of observations for each field (N_f).
8. t_0 : Initial time of the KN transient, which corresponds to the initial absolute magnitude M_0
9. $\bar{f}$: Index for fields not including the field f.
10. $\bar{F}$: Hypothesis that the KN is not in any of the observed fields.
11. A : Hypothesis that the event is of astrophysical origin.
12. T : Hypothesis that the event is of terrestrial origin (implying that the event is spurious).
13. $P^i(A)$: The probability of the ith event being of astrophysical (A) origin.
14. $\{d^i\}$: The set of EM data associated with all events, indexed by i. The data is indexed by the field index f and time of observation index j. We take our data to be the set of limiting (apparent) magnitudes $\{m_l^{i,f,j}\}$ in each field at the given time of observation.

Multiple observations and their corresponding observation times would independently constrain the model. Taking into account this and the astrophysical hypothesis A, the likelihood term for each field is derived to be:

$$
\begin{aligned}
p(\{d^i\}|M_0,\,\alpha) = \prod_{i=1}^{N_E} \Bigg[& \Bigg(\sum_{f=1}^{N_F} \Bigg(\prod_{j=1}^{N_f} p(m_l^{i,f,j}|M_0,\,\alpha,\,A,\,f) \\
& \times \prod_{\substack{\bar{f}=1,\\ \bar{f}\neq f}}^{N_F} p(m_l^{i,\bar{f}}|A,f)P(f) \Bigg) \\
& + \prod_f p(m_l^{i,f}|A,\,\bar{F}) \Bigg(1 - \sum_{f=1}^{N_F} P(f) \Bigg) \Bigg) P^i(A) \\
& + \prod_f p(m_l^{i,f}|T)(1 - P^i(A)) \Bigg]
\end{aligned}
\tag{E1}
$$

Normalizing the likelihood term, and the terms for the field (f), non-field (f) and terrestrial (T) hypotheses, we simplify Equation (E1) to get the posterior:

$$
\begin{aligned}
p(M_0,\,\alpha|\{d^i\}) \propto \prod_{i=1}^{N_E} \Bigg[& \Bigg(\sum_{f=1}^{N_F} \Bigg(\frac{\prod_j p(m_l^{i,f,j}|M_0,\,\alpha,\,A,\,f)}{\prod_j p(m_l^{i,f,j}|A,\,\bar{f})} \Bigg) P(f) \\
& + \Bigg(1 - \sum_{f=1}^{N_F} P(f) \Bigg) \Bigg) P^i(A) + (1 - P^i(A)) \Bigg] p(M_0,\,\alpha)
\end{aligned}
\tag{E2}
$$

Appendix F
Candidates Not Discussed in this Paper

In Table 3 we show the candidates that were not part of this paper, as they were not accessible from Palomar.

Table 3
Candidates Not Accessible from Palomar

Team	AT Name	R.A. (deg)	Decl. (deg)	Δt	Discovery mag. (AB magnitude)	Credible Region
GW-MMADS	AT2025bnx	243.198339	−68.827761	6.43	$r = 20.53$ mag	0.45
GW-MMADS	AT2025bnl	242.330798	−69.341945	6.38	$i = 21.34$ mag	0.45
GW-MMADS	AT2025bnm	245.717365	−69.023307	6.39	$i = 22.10$ mag	0.46
GW-MMADS	AT2025bno	242.698474	−68.470445	6.38	$i = 21.11$ mag	0.49
GW-MMADS	AT2025bnh	248.159200	−68.517481	6.40	$i = 21.45$ mag	0.50
SOAR	AT2025ber	247.960000	−69.528969	0.44	$i = 22.00$ mag	0.50
GW-MMADS	AT2025boa	238.313614	−69.284913	6.38	$i = 21.50$ mag	0.50
GW-MMADS	AT2025bni	248.497050	−69.302599	6.40	$i = 22.50$ mag	0.51
GW-MMADS	AT2025bmx	239.335215	−68.667346	6.38	$i = 20.70$ mag	0.52
GW-MMADS	AT2025btp	243.285298	−68.054332	6.39	$i = 21.96$ mag	0.52
GW-MMADS	AT2025bnt	248.456112	−70.049160	6.39	$i = 21.36$ mag	0.52
GW-MMADS	AT2025bnn	246.087141	−67.969303	6.39	$i = 21.64$ mag	0.52
GW-MMADS	AT2025btg	245.808953	−67.950089	6.40	$i = 21.31$ mag	0.54
GW-MMADS	AT2025bnp	238.092561	−70.078637	6.38	$i = 21.14$ mag	0.54
GW-MMADS	AT2025bng	237.311207	−68.793026	6.37	$i = 21.33$ mag	0.54
GW-MMADS	AT2025bmt	241.702375	−68.015378	6.38	$i = 20.95$ mag	0.54
GW-MMADS	AT2025bna	250.352179	−69.852791	6.40	$i = 22.09$ mag	0.54
GW-MMADS	AT2025bnz	252.642449	−69.271086	6.41	$i = 21.03$ mag	0.56
GW-MMADS	AT2025bne	241.735013	−67.822171	6.38	$i = 21.08$ mag	0.56
GW-MMADS	AT2025bnu	252.865009	−69.107941	6.41	$i = 21.40$ mag	0.56
GW-MMADS	AT2025bmr	253.039696	−69.238089	6.41	$i = 20.04$ mag	0.56
GW-MMADS	AT2025bns	253.108277	−69.071872	6.41	$i = 22.20$ mag	0.56
GW-MMADS	AT2025bth	253.015441	−68.239550	6.48	$i = 20.25$ mag	0.57
GW-MMADS	AT2025bnb	237.554278	−70.317931	6.37	$i = 20.61$ mag	0.57
GW-MMADS	AT2025bnd	241.490340	−67.782256	6.38	$i = 22.02$ mag	0.57
GW-MMADS	AT2025bmv	241.482057	−67.782698	6.39	$i = 22.20$ mag	0.57
GW-MMADS	AT2025bob	239.568537	−67.947727	6.38	$i = 21.66$ mag	0.57
GW-MMADS	AT2025bmy	235.654159	−69.613801	6.37	$i = 20.83$ mag	0.57
GW-MMADS	AT2025bnw	235.314005	−69.511897	6.37	$i = 22.29$ mag	0.57
GW-MMADS	AT2025bnk	236.684850	−68.624928	6.37	$i = 20.30$ mag	0.58
GW-MMADS	AT2025bmu	242.175587	−67.502065	6.39	$i = 21.60$ mag	0.58
GW-MMADS	AT2025bti	239.814737	−67.758628	6.38	$i = 21.70$ mag	0.59
GW-MMADS	AT2025btr	254.511807	−68.447070	6.48	$i = 22.29$ mag	0.59
GW-MMADS	AT2025bms	247.101545	−70.816131	6.40	$i = 21.37$ mag	0.59
GW-MMADS	AT2025btc	241.670680	−70.991068	6.39	$i = 22.11$ mag	0.61
GW-MMADS	AT2025btl	250.676560	−67.511204	6.47	$i = 22.44$ mag	0.61
GW-MMADS	AT2025btm	247.969931	−71.211799	6.40	$i = 21.38$ mag	0.61
GW-MMADS	AT2025bnf	252.514939	−70.593309	6.41	$i = 20.33$ mag	0.62
GW-MMADS	AT2025bte	247.408084	−71.315427	6.40	$i = 20.92$ mag	0.63
GW-MMADS	AT2025bnc	256.260785	−69.873825	6.41	$i = 22.25$ mag	0.65
GW-MMADS	AT2025bnv	235.926019	−67.682568	6.38	$i = 20.89$ mag	0.65
GW-MMADS	AT2025btj	241.632510	−66.959770	6.38	$i = 22.05$ mag	0.65
GW-MMADS	AT2025bnr	239.310711	−67.192893	6.38	$i = 21.09$ mag	0.66
GW-MMADS	AT2025btq	237.204147	−67.313042	6.38	$i = 21.96$ mag	0.66
GW-MMADS	AT2025btk	232.860157	−68.779324	6.37	$i = 20.47$ mag	0.67
GW-MMADS	AT2025btd	255.847308	−70.370222	6.41	$i = 20.64$ mag	0.68
GW-MMADS	AT2025bnj	239.962646	−66.929715	6.38	$i = 20.87$ mag	0.68
GW-MMADS	AT2025bmz	250.110134	−66.773856	6.43	$r = 19.39$ mag	0.68

Table 3
(Continued)

Team	AT Name	R.A. (deg)	Decl. (deg)	Δt	Discovery mag. (AB magnitude)	Credible Region
GOTO	AT2025bau	253.166158	−66.813549	0.86	$L = 19.59$ mag	0.73
GW-MMADS	AT2025btn	232.587844	−70.411893	6.37	$i = 19.17$ mag	0.76
GW-MMADS	AT2025bnq	237.860041	−71.709022	6.37	$i = 20.75$ mag	0.76
GW-MMADS	AT2025bts	251.287795	−71.523116	6.41	$i = 22.58$ mag	0.77
GW-MMADS	AT2025bmw	244.552812	−71.938206	6.40	$i = 20.78$ mag	0.78
GW-MMADS	AT2025bto	237.129581	−71.826170	6.37	$i = 21.56$ mag	0.81
GW-MMADS	AT2025bny	238.070346	−72.142874	6.37	$i = 20.62$ mag	0.85
GOTO	AT2025cat	262.154143	−68.789674	10.84	$L = 18.63$ mag	0.87
GW-MMADS	AT2025btf	235.928949	−71.902516	6.42	$r = 21.25$ mag	0.88
GOTO	AT2025bao	169.237933	−45.541262	0.58	$L = 19.14$ mag	0.93
GOTO	AT2025bar	170.681922	−45.574606	0.69	$L = 20.23$ mag	0.94
ATLAS	AT2025bfg	184.400370	−59.493302	5.12	orange = 18.53 mag	0.95

Appendix G
Models Ruled Out

In this section we show the corner plot fo the models from Section 4 that were ruled out (see Figures 12–15).

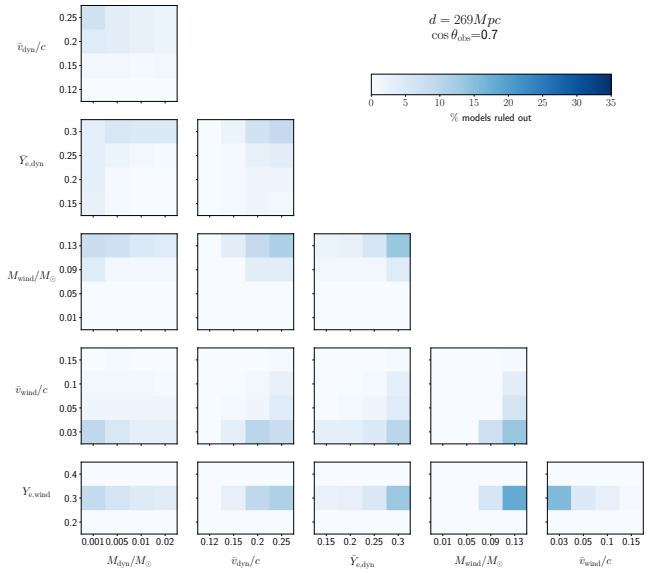

Figure 12. Corner plot showing in a colorbar the percentage of BNS models ruled out at a fixed distance of 269 Mpc and at a fixed viewing angle of 45°. The parameters correspond to the ejecta mass, mass-weighted averaged velocity and mass-weighted electron fraction for the dynamical and wind ejecta: $m_{\rm dyn}$, $\bar{v}_{\rm dyn}$, $\bar{Y}_{\rm e,dyn}$, $m_{\rm wind}$, $\bar{v}_{\rm wind}$ and $\bar{Y}_{\rm e,wind}$.

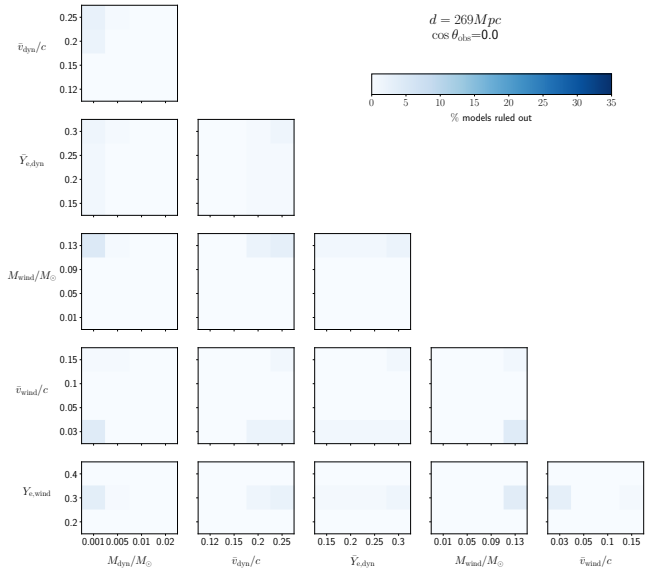

Figure 13. Corner plot showing in a colorbar the percentage of BNS models ruled out at a fixed distance of 269 Mpc and at a fixed viewing angle of 90°. The parameters correspond to the ejecta mass, mass-weighted averaged velocity and mass-weighted electron fraction for the dynamical and wind ejecta: $m_{\rm dyn}$, $\bar{v}_{\rm dyn}$, $\bar{Y}_{\rm e,dyn}$, $m_{\rm wind}$, $\bar{v}_{\rm wind}$ and $\bar{Y}_{\rm e,wind}$.

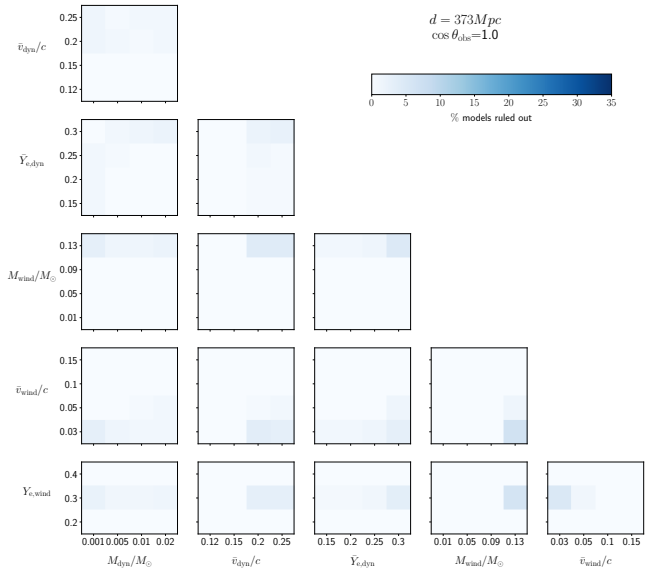

Figure 14. Corner plot showing in a colorbar the percentage of BNS models ruled out at a fixed distance of 373 Mpc and at a fixed viewing angle of 0°. The parameters correspond to the ejecta mass, mass-weighted averaged velocity and mass-weighted electron fraction for the dynamical and wind ejecta: $m_{\rm dyn}$, $\bar{v}_{\rm dyn}$, $\bar{Y}_{\rm e,dyn}$, $m_{\rm wind}$, $\bar{v}_{\rm wind}$ and $\bar{Y}_{\rm e,wind}$.

ORCID iDs

Tomás Ahumada https://orcid.org/0000-0002-2184-6430
Shreya Anand https://orcid.org/0000-0003-3768-7515
Mattia Bulla https://orcid.org/0000-0002-8255-5127
Vaidehi Gupta https://orcid.org/0000-0002-7672-0480

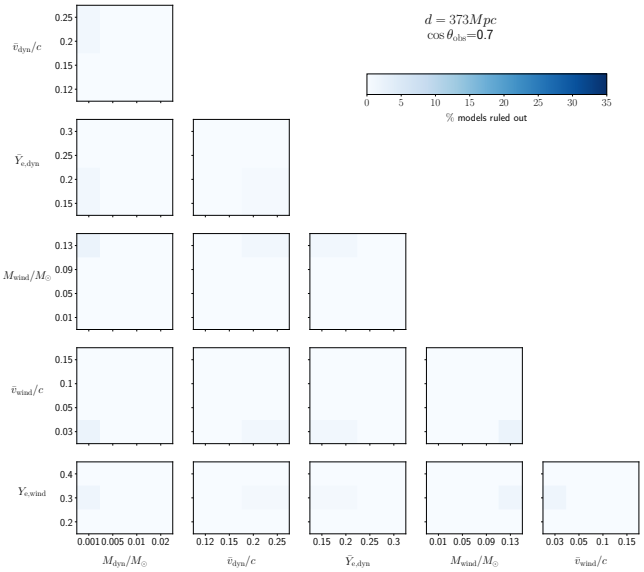

Figure 15. Corner plot showing in a colorbar the percentage of BNS models ruled out at a fixed distance of 269 Mpc and at a fixed viewing angle of 45°. The parameters correspond to the ejecta mass, mass-weighted averaged velocity and mass-weighted electron fraction for the dynamical and wind ejecta: $m_{\rm dyn}$, $\bar{v}_{\rm dyn}$, $\bar{Y}_{\rm e,dyn}$, $m_{\rm wind}$, $\bar{v}_{\rm wind}$ and $\bar{Y}_{\rm e,wind}$.

Mansi Kasliwal https://orcid.org/0000-0002-5619-4938
Robert Stein https://orcid.org/0000-0003-2434-0387
Viraj Karambelkar https://orcid.org/0000-0003-2758-159X
Eric C. Bellm https://orcid.org/0000-0001-8018-5348
Theophile Jegou du Laz https://orcid.org/0009-0003-6181-4526
Michael W. Coughlin https://orcid.org/0000-0002-8262-2924
Igor Andreoni https://orcid.org/0000-0002-8977-1498
Smaranika Banerjee https://orcid.org/0000-0001-6595-2238
Aleksandra Bochenek https://orcid.org/0009-0008-2714-2507
K-Ryan Hinds https://orcid.org/0000-0002-0129-806X
Lei Hu https://orcid.org/0000-0001-7201-1938
Antonella Palmese https://orcid.org/0000-0002-6011-0530
Daniel Perley https://orcid.org/0000-0001-8472-1996
Natalya Pletskova https://orcid.org/0009-0008-8062-445X
Anirudh Salgundi https://orcid.org/0000-0003-3173-4691
Avinash Singh https://orcid.org/0000-0003-2091-622X
Jesper Sollerman https://orcid.org/0000-0003-1546-6615
Vishwajeet Swain https://orcid.org/0000-0002-7942-8477
Avery Wold https://orcid.org/0000-0002-9998-6732
Varun Bhalerao https://orcid.org/0000-0002-6112-7609
S. Bradley Cenko https://orcid.org/0000-0003-1673-970X
David O. Cook https://orcid.org/0000-0002-6877-7655
Chris Copperwheat https://orcid.org/0000-0001-7983-8698
Matthew Graham https://orcid.org/0000-0002-3168-0139
David L. Kaplan https://orcid.org/0000-0001-6295-2881

Leo P. Singer https://orcid.org/0000-0001-9898-5597
Malte Busmann https://orcid.org/0009-0001-0574-2332
Julius Gassert https://orcid.org/0009-0008-2754-1946
Daniel Gruen https://orcid.org/0000-0003-3270-7644
Julian Sommer https://orcid.org/0000-0002-1154-8317
Yajie Zhang https://orcid.org/0000-0003-2976-8198
Ariel Amsellem https://orcid.org/0000-0003-3433-2698
Tomás Cabrera https://orcid.org/0000-0002-1270-7666
Xander J. Hall https://orcid.org/0000-0002-9364-5419
Keerthi Kunnumkai https://orcid.org/0009-0000-4830-1484
Brendan O'Connor https://orcid.org/0000-0002-9700-0036
Tyler Barna https://orcid.org/0000-0002-4843-345X
Felipe Fontinele Nunes https://orcid.org/0000-0001-7129-1325
Andrew Toivonen https://orcid.org/0009-0008-9546-2035
Argyro Sasli https://orcid.org/0000-0001-7357-0889
Frank J. Masci https://orcid.org/0000-0002-8532-9395
Tracy X. Chen https://orcid.org/0000-0001-9152-6224
Richard Dekany https://orcid.org/0000-0002-5884-7867
Josiah Purdum https://orcid.org/0000-0003-1227-3738
Antoine Le Calloch https://orcid.org/0009-0009-7000-8343
G. C. Anupama https://orcid.org/0000-0003-3533-7183
Sudhanshu Barway https://orcid.org/0000-0002-3927-5402

References

Abbott, B. P., Abbott, R., Abbott, T. D., et al. 2017a, ApJL, 848, L13
Abbott, R., Abbott, T. D., Acernese, F., et al. 2023, PhRvX, 13, 041039
Abbott, B. P., Abbott, R., Abbott, T. D., et al. 2017b, PhRvL, 119, 161101
Ackley, K., Belkin, S., Steeghs, D., et al. 2025, GCN, 39197, 1
Ahumada, T., Anand, S., Coughlin, M. W., et al. 2022, ApJ, 932, 40
Ahumada, T., Anand, S., Coughlin, M. W., et al. 2024, PASP, 136, 114201
Ahumada, T., Karambelkar, V., Bellm, E., et al. 2025, GCN, 39228, 1
Ahumada, T., Singer, L. P., Anand, S., et al. 2021, NatAs, 5, 917
Akmal, A., Pandharipande, V. R., & Ravenhall, D. G. 1998, PhRvC, 58, 1804
Alexander, K. D., Schroeder, G., Paterson, K., et al. 2021, ApJ, 923, 66
Anand, S., Coughlin, M. W., Kasliwal, M. M., et al. 2021, NatAs, 5, 46
Anand, S., Pang, P. T. H., Bulla, M., et al. 2023, arXiv:2307.11080
Andreoni, I., Coughlin, M. W., Kool, E. C., et al. 2021, ApJ, 918, 63
Andreoni, I., Goldstein, D. A., Anand, S., et al. 2019, ApJL, 881, L16
Andreoni, I., Goldstein, D. A., Kasliwal, M. M., et al. 2020, ApJ, 890, 131
Antier, S., Agayeva, S., Almualla, M., et al. 2020, MNRAS, 497, 5518
Arcavi, I. 2018, ApJL, 855, L23
Ashton, G., Hübner, M., Lasky, P. D., et al. 2019, ApJS, 241, 27
Balasubramanian, A., Corsi, A., Mooley, K. P., et al. 2022, ApJ, 938, 12
Banerjee, S., Tanaka, M., Kato, D., et al. 2022, ApJ, 934, 117
Becerra, R. L., Dichiara, S., Watson, A. M., et al. 2025, GCN, 39208, 1
Beck, R., Dobos, L., Budavári, T., Szalay, A. S., & Csabai, I. 2016, MNRAS, 460, 1371
Bellm, E. C., Kulkarni, S. R., Graham, M. J., et al. 2019, PASP, 131, 018002
Bellm, E. C., & Sesar, B. 2016, pyraf-dbsp: Reduction pipeline for the Palomar Double Beam Spectrograph, Astrophysics Source Code Library, ascl:1602.002
Bertin, E., & Arnouts, S. 2010, SExtractor: Source Extractor, Astrophysics Source Code Library, ascl:1010.064
Blagorodnova, N., Neill, J. D., Walters, R., et al. 2018, PASP, 130, 035003
Boubert, D., & Everall, A. 2020, MNRAS, 497, 4246
Bulla, M. 2019, MNRAS, 489, 5037
Bulla, M. 2023, MNRAS, 520, 2558
Busmann, M., Gruen, D., O'Connor, B., et al. 2025a, GCN, 39214, 1
Busmann, M., O'Connor, B., Sommer, J., et al. 2025b, A&A, 701, A225
Cabrera, T., Hu, L., Hall, X., et al. 2025, GCN, 39318, 1
Cabrera, T., Palmese, A., Hu, L., et al. 2024, PhRvD, 110, 123029
Chambers, K. C., Magnier, E. A., Metcalfe, N., et al. 2016, arXiv:1612.05560
Chatterjee, D., Ghosh, S., Brady, P. R., et al. 2020, ApJ, 896, 54
Chen, H.-Y., Zeimann, G., Wheeler, J. C., Vinko, J. & Lighetr Collaboration 2025a, GCN, 39785, 1
Chen, T. W., Aryan, A., Yang, S., et al. 2025b, GCN, 39285, 1
Chime/Frb Collaboration 2025, GCN, 39216, 1
Coughlin, M. W., Ahumada, T., Cenko, S. B., et al. 2019b, PASP, 131, 048001
Coughlin, M. W., Bloom, J. S., Nir, G., et al. 2023, ApJS, 267, 31
Coughlin, M. W., Ahumada, T., Anand, S., et al. 2019a, ApJL, 885, L19
Coughlin, M. W., Tao, D., Chan, M. L., et al. 2018, MNRAS, 478, 692
Coulter, D. A., Kilpatrick, C. D., Macias, P., et al. 2025, GCN, 39234, 1
Coulter, D. A., Foley, R. J., Kilpatrick, C. D., et al. 2017, Sci, 358, 1556
de Wet, S., Groot, P. J., Bloemen, S., et al. 2021, A&A, 649, A72
Dekany, R., Smith, R. M., Riddle, R., et al. 2020, PASP, 132, 038001
Dietrich, T., Coughlin, M. W., Pang, P. T. H., et al. 2020, Sci, 370, 1450
Dobie, D., Stewart, A., Hotokezaka, K., et al. 2022, MNRAS, 510, 3794
Drago, A., Lavagno, A., Pagliara, G., & Pigato, D. 2014, PhRvC, 90, 065809
Drout, M. R., Piro, A. L., Shappee, B. J., et al. 2017, Sci, 358, 1570
Duev, D. A., Mahabal, A., Masci, F. J., et al. 2019, MNRAS, 489, 3582
Evans, P. A., Cenko, S. B., Kennea, J. A., et al. 2017, Sci, 358, 1565
Fortin, F., Watson, A. M., Antier, S., et al. 2025, GCN, 39226, 1
Freeburn, J., Carney, J., Andreoni, I., & Cook, D. 2025, GCN, 39196, 1
Fremling, C., Sollerman, J., Taddia, F., et al. 2016, A&A, 593, A68
Frostig, D., Karambelkar, V. R., Stein, R. D., et al. 2025, PASP, 137, 074203
Gaia Collaboration 2018, yCat, I/345
Gaia Collaboration, Vallenari, A., Brown, A. G. A., et al. 2023, A&A, 674, A1
Goldstein, A., Veres, P., Burns, E., et al. 2017, ApJL, 848, L14
Goldstein, D. A., Andreoni, I., Nugent, P. E., et al. 2019, ApJL, 881, L7
Gompertz, B. P., Cutter, R., Steeghs, D., et al. 2020, MNRAS, 497, 726
Gössl, C. A., & Riffeser, A. 2002, A&A, 381, 1095
Graham, M. J., Kulkarni, S. R., Bellm, E. C., et al. 2019, PASP, 131, 078001
Guevel, D., & Hosseinzadeh, G. 2017, Dguevel/Pyzogy: Initial Release, v0.0.1, Zenodo, doi:10.5281/zenodo.1043973
Haggard, D., Nynka, M., Ruan, J. J., et al. 2017, ApJL, 848, L25
Hallinan, G., Corsi, A., Mooley, K. P., et al. 2017, Sci, 358, 1579
Hempel, M., & Schaffner-Bielich, J. 2010, NuPhA, 837, 210
Hopp, U., Bender, R., Grupp, F., et al. 2014, SPIE, 9145, 91452D
Hosseinzadeh, G., Shrestha, M., Sand, D. J., et al. 2025, GCN, 39191, 1
Hu, L., Cabrera, T., Palmese, A., et al. 2025, ApJ, 990, L46
Hu, Y. D., Fernández-García, E., Caballero-García, M. D., et al. 2023, FrASS, 10, 952887
Huber, M. E., Gillanders, J. H., Chambers, K., et al. 2025a, GCN, 39272, 1
Huber, M. E., Gillanders, J. H., Chambers, K. C., et al. 2025b, GCN, 39195, 1
IceCube Collaboration 2025, GCN, 39176, 1
Karambelkar, V., Ahumada, T., Kasliwal, M. & Ztf CollaborationGrowth Collaboration 2025a, GCN, 39229, 1
Karambelkar, V., Ahumada, T., Rose, S., et al. 2025b, GCN, 39273, 1
Kasen, D., Metzger, B., Barnes, J., Quataert, E., & Ramirez-Ruiz, E. 2017, Natur, 551, 80
Kasliwal, M. M., Anand, S., Ahumada, T., et al. 2020, ApJ, 905, 145
Kasliwal, M. M., Cannella, C., Bagdasaryan, A., et al. 2019, PASP, 131, 038003
Kasliwal, M. M., Kasen, D., Lau, R. M., et al. 2019, MNRAS, 510, L7
Kasliwal, M. M., Nakar, E., Singer, L. P., et al. 2017, Sci, 358, 1559
Kawaguchi, K., Shibata, M., & Tanaka, M. 2020, ApJ, 889, 171
Kilpatrick, C. D., Coulter, D. A., Arcavi, I., et al. 2021, ApJ, 923, 258
Kim, Y. L., Rigault, M., Neill, J. D., et al. 2022, PASP, 134, 024505
Kumar, H., Bhalerao, V., Anupama, G. C., et al. 2022, AJ, 164, 90
Lang-Bardl, F., Bender, R., Goessl, C., et al. 2016, SPIE, 9908, 990844
Levan, A. 2020, PoS, Asterics2019, 044

Li, D. Y., Hu, J. W., Wu, Q. Y., et al. 2025, GCN, 39545, 1
Ligo Scientific Collaboration, VIRGO Collaboration, & Kagra Collaboration 2025a, GCN, 39178, 1
Ligo Scientific Collaboration, VIRGO Collaboration, & Kagra Collaboration 2025b, GCN, 39175, 1
Ligo Scientific Collaboration, VIRGO Collaboration, & Kagra Collaboration 2025c, GCN, 39231, 1
Lipunov, V., Gorbovskoy, E., Kuznetsov, A., et al. 2025, GCN, 39265, 1
Lipunov, V. M., Gorbovskoy, E., Kornilov, V. G., et al. 2017, ApJL, 850, L1
Liu, Z. Y., He, L., Zhao, W., et al. 2025, GCN, 39249, 1
Lundquist, M. J., Paterson, K., Fong, W., et al. 2019, ApJL, 881, L26
Makhathini, S., Mooley, K. P., Brightman, M., et al. 2021, ApJ, 922, 154
Margutti, R., Berger, E., Fong, W., et al. 2017, ApJL, 848, L20
Masci, F. J., Laher, R. R., Rusholme, B., et al. 2019, PASP, 131, 018003
Mathias, L. W. P., Di Clemente, F., Bulla, M., & Alessandro, D. 2024, MNRAS, 527, 11053
Mohite, S. R., Rajkumar, P., Anand, S., et al. 2022, ApJ, 925, 58
Mooley, K. P., Anderson, J., & Lu, W. 2022, Natur, 610, 273
Mooley, K. P., Deller, A. T., Gottlieb, O., et al. 2018, Natur, 561, 355
Morgan, R., Soares-Santos, M., Annis, J., et al. 2020, ApJ, 901, 83
Morisaki, S., Smith, R., Tsukada, L., et al. 2023, PhRvD, 108, 123040
Nakar, E. 2020, PhR, 886, 1
Nordin, J., Brinnel, V., van Santen, J., et al. 2019, A&A, 631, A147
Paek, G. S. H., Im, M., Jeong, M., et al. 2025, GCN, 39241, 1
Paek, G. S. H., Im, M., Kim, J., et al. 2024, ApJ, 960, 113
Patterson, M. T., Bellm, E. C., Rusholme, B., et al. 2019, PASP, 131, 018001
Perego, A., Radice, D., & Bernuzzi, S. 2017, ApJL, 850, L37
Perley, D. A. 2019, PASP, 131, 084503
Perley, D. A., Ho, A. Y. Q., Fausnaugh, M., et al. 2025, MNRAS, 537, 1
Pillas, M., Antier, S., Ackley, K., et al. 2025, PhRvD, 112, 083002
Pozanenko, A. S., Barkov, M. V., Minaev, P. Y., et al. 2018, ApJL, 852, L30
Prochaska, J. X., Hennawi, J., Cooke, R., et al. 2020a, pypeit/PypeIt: Release v1.0.0, Zenodo, doi:10.5281/zenodo.3743493
Prochaska, J., Hennawi, J., Westfall, K., et al. 2020b, JOSS, 5, 2308
Prochaska, J. X., Hennawi, J. F., Westfall, K. B., et al. 2020c, JOSS, 5, 2308
Radice, D., Perego, A., Hotokezaka, K., et al. 2018, ApJ, 869, 130
Rastinejad, J. C., Paterson, K., Fong, W., et al. 2022, ApJ, 927, 50
Rigault, M., Neill, J. D., Blagorodnova, N., et al. 2019, A&A, 627, A115
Rosswog, S., & Korobkin, O. 2024, AnP, 536, 2200306
Setzer, C. N., Peiris, H. V., Korobkin, O., & Rosswog, S. 2023, MNRAS, 520, 2829
Shappee, B. J., Prieto, J. L., Grupe, D., et al. 2014, ApJ, 788, 48
Singer, L. P., & Price, L. R. 2016, PhRvD, 93, 024013
Smith, K. W., Angus, C. R., Young, D. R., et al. 2025, GCN, 39211, 1
Soares-Santos, M., Holz, D., Annis, J., Chornock, R., & Herner, K. 2017, ApJ, 848, L16
Steeghs, D., Ackley, K., Kennedy, M., et al. 2025, GCN, 39215, 1
Steele, I. A., Smith, R. J., Rees, P. C., et al. 2004, SPIE, 5489, 679
Stein, R., Karambelkar, V., Frostig, D., et al. 2025, GCN, 39256, 1
Stein, R., Reusch, S., Franckowiak, A., et al. 2023a, MNRAS, 521, 5046
Stein, R., Reusch, S., & Necker, J. 2023b, desy-multimessenger/nuztf: v2.7.1 Release, Zenodo, doi:10.5281/zenodo.7990902
Tachibana, & Miller 2018, PASP, 130, 128001
Thakur, A. L., Dichiara, S., Troja, E., et al. 2021, MNRAS, 501, 2821
Tonry, J. L., Denneau, L., Heinze, A. N., et al. 2018, PASP, 130, 064505
Troja, E., Piro, L., van Eerten, H., et al. 2017, Natur, 551, 71
Tucker, D. L., Wiesner, M. P., Allam, S. S., et al. 2022, ApJ, 929, 115
Utsumi, Y., Tanaka, M., Tominaga, N., et al. 2017, PASJ, 69, 101
Valenti, S., David, J. S., Yang, S., et al. 2017, ApJ, 848, L24
van der Walt, S. J., Crellin-Quick, A., & Bloom, J. S. 2019, JOSS, 4, 1247
Vieira, N., Ruan, J. J., Haggard, D., et al. 2020, ApJ, 895, 96
Watson, A. M., Ducoin, J.-G., Antier, S., et al. 2025, GCN, 39193, 1
Weizmann Kiendrebeogo, R., Farah, A. M., Foley, E. M., et al. 2023, ApJ, 958, 158
Wright, E. L., Eisenhardt, P. R. M., Mainzer, A. K., et al. 2010, AJ, 140, 1868
Wyatt, S. D., Tohuvavohu, A., Arcavi, I., et al. 2020, ApJ, 894, 127
Yao, Y., De, K., Kasliwal, M. M., et al. 2020, ApJ, 900, 46
Young, D. R., Gillanders, J. H., Huber, M. E., et al. 2025, GCN, 39210, 1
Zackay, B., Ofek, E. O., & Gal-Yam, A. 2016, ApJ, 830, 27
Zhou, R., Newman, J. A., Mao, Y.-Y., et al. 2021, MNRAS, 501, 3309